



# A multi-horizon fully coupled thermo-mechanical peridynamics

Changyi Yang<sup>a</sup>, Fan Zhu<sup>b</sup>, Jidong Zhao<sup>a,c,\*</sup>

<sup>a</sup> Department of Civil and Environmental Engineering, The Hong Kong University of Science and Technology, HKSAR, China

<sup>b</sup> Department of Urban Management, Kyoto University, Kyoto, Japan

<sup>c</sup> State Key Laboratory of Mountain Hazards and Engineering Resilience, Chengdu, Sichuan, China

## ARTICLE INFO

### Keywords:

Multi-physics  
Peridynamics  
Coupling  
Thermal fracture  
Computational modeling

## ABSTRACT

This paper presents a fully coupled thermo-mechanical peridynamic model for simulating interactive thermo-mechanical material responses and thermally induced fracturing of solids. A temperature-dependent constitutive model and a deformation-dependent heat conduction model are derived for state-based peridynamic formulation. The dispersion relation and truncation error of the state-based peridynamic heat equation are analyzed for the first time. It is found that as non-locality becoming more pronounced, the dissipative rate of heat is reduced, and the truncation error becomes larger. A small horizon can effectively mitigate oscillation while reducing the error in the temperature field. For coupled thermo-mechanical modeling, a novel multi-horizon scheme is introduced where the thermal field is solved with a different horizon than that of the mechanical field. The multi-horizon scheme allows for the implementation of a distinct degree of non-locality for different physical field. Comparing with the constant-horizon scheme, we demonstrate through numerical examples that the multi-horizon scheme offers smoother and more accurate solutions and serves a promising option for peridynamics-based multi-physics simulations.

## 1. Introduction

The peridynamic (PD) theory (Silling, 2000; Silling et al., 2007) is a non-local extension of the classical continuum mechanics. It is based on integral-differentiation governing equations which make it inherently suitable for modeling discontinuities. The method has gained increasing popularity in modeling fracturing in solids (Gao and Oterkus, 2019; Liu et al., 2024; Shi et al., 2022; Wan et al., 2020; Yang et al., 2024; Zhu and Zhao, 2019a, 2019b; 2021). Nonetheless, fracturing in many natural and industrial processes is accompanied by multiphysics processes. Thermal fracturing is one of the examples. It is regarded as one of the weathering mechanisms of rock (Buckman et al., 2021) and is also one of the most devastating defects in additive manufacturing (Ruan et al., 2023). In geothermal energy exploitation, cool water is often injected into hot rock to build large scale crack networks to improve the heat extract efficiency (Xue et al., 2023). The thermal fracturing is not an independent process but is fully coupled with the mechanical response of material. It is well known that mutual influence of the temperature variation and material deformation exists.

Given the advantages of the PD theory in modeling discontinuities, it is natural to develop a coupled thermo-mechanical (TM) PD for modeling the interacting thermal and mechanical fields associated with the fracturing process. Pioneering works on TM PD include Kilic and Madenci (2010), Agwai (2011), and Oterkus et al. (2014a, 2014b), who developed PD heat conduction equation and

\* Corresponding author at: Department of Civil and Environmental Engineering, The Hong Kong University of Science and Technology, HKSAR, China.

E-mail address: [jzhao@ust.hk](mailto:jzhao@ust.hk) (J. Zhao).

<https://doi.org/10.1016/j.jmps.2024.105758>

Received 3 April 2024; Received in revised form 8 June 2024; Accepted 27 June 2024

Available online 28 June 2024

0022-5096/© 2024 Elsevier Ltd. All rights are reserved, including those for text and data mining, AI training, and similar technologies.

subsequently fully coupled PD thermomechanics based on the irreversible thermodynamics. Both the equation of motion and thermal diffusion are formulated with bond-based PD. More recently, the thermomechanical framework is extended to ordinary state-based (Zhang and Qiao, 2018, 2020) and non-ordinary state-based (Sun et al., 2023) ones. However, the heat equation is not explicitly included in these analyses, and only the one-way effects of temperature on stress are considered. With these coupled thermo-mechanical methods, PD has been employed to simulate thermal cracking of various brittle materials including rocks, concretes, ice and ceramics (Wang et al., 2019; Bazazzadeh et al., 2020; Chen et al., 2021; Song et al., 2022; Sun et al., 2023; Song et al., 2021; Zhang et al., 2023). It is worth noting that PD is a versatile computational framework that can integrate multiple physical fields. Examples include coupled hydro-mechanical/thermo-hydro-mechanical modeling for porous media (Oterkus et al., 2017; Song and Silling, 2020; Menon and Song, 2021, 2022, 2023; Ni et al., 2022, 2023; Yu et al., 2024a, b, c), fluid-driven fracturing (Sun et al., 2022a; Sun et al., 2022b; Yang et al., 2024), and ion diffusion and chemical reactions (Chen and Bobaru, 2015; Wang et al., 2018a; Wu and Chen, 2023; Yang et al., 2020).

The PD theory is known to be a non-local theory, meaning that a material point interacts not only with its immediate neighboring points but also points at a finite distance, namely the *horizon*. This non-locality enables PD to well capture the crack propagation process in fracturing problems. However, when incorporating different physical fields except the mechanical field in the PD framework, it is important to realize that the non-local nature of PD may become a possible source of error, since many physical processes are governed by local equilibrium. For heat conduction problems, for example, the transfer of heat occurs through direct contact between adjacent materials and such process is described by the local governing equations in classical thermodynamics. However, when simulating either pure heat conduction or couple thermo-mechanical problems in PD, the heat transfer is still modeled within a finite zone of influence. Hence, the point-skipping heat transfer contradicts the physics underlying actual conduction when observed from a macroscopic perspective. The parametric studies conducted by Agwai (2011) reveal that the temperature distribution significantly deviates from the analytical solution as the horizon becomes larger. Moreover, the PD formulation is found to be dispersive. When modeling mechanical responses of materials, dispersion occurs for high frequency waves mainly owing to the non-local nature of PD and it may also be attributed to discretization (Bessa et al., 2014; Bažant et al., 2016; Butt et al., 2017). When modeling fluid flow in porous media using PD, Ni et al., (2022) analyzed the length scale of different phases and mentioned that dispersive behavior may occur due to the Laplacian term in Darcy’s law. In view of the similarity between Fourier’s law and Darcy’s law, when applying PD for modeling the thermal field, numerical issues such as oscillation of field variables and dispersion of thermal waves can be expected. However, to the best knowledge of the authors, no prior investigation has been performed to address dispersion characters and error mitigation for PD formulation of the heat conduction equation.

For the thermo-mechanical model within pure PD framework, most of the existing methods are developed within the framework of bond-based PD, which assumes that bonds behave independently from each other. Potential drawbacks of the bond-based PD have been discussed in detail by Silling et al. (2007) including limitation on the Poisson’s ratio of materials and difficulties in incorporating complex constitutive behavior of materials. When modeling heat conduction by bond-based PD, a micro-conductivity is always needed to make analogy between classical material conductivity and peridynamic material conductivity. However, the determination of this parameter itself is non-trivial since it depends on the weight function. Either complicated analytical expression or numerical calculation of this parameter is needed. These drawbacks associated with the bond-based PD can be greatly eased by adopting the state-based PD. Notably, Ni et al. (2023) recently employed the state-based PD to model mechanical response of the solid phase and finite element method (FEM) to model heat conduction and fluid flow in porous media, with additional coupling techniques introduced between PD and FEM.

The objective of this work is to present a fully coupled thermo-mechanical formulation suited for the state-based PD, with rigorous study of its dispersion characters and discretization-induced error. For the coupling between the thermal and mechanical fields, we show derivation of a temperature-dependent elastic model together with a deformation-dependent heat conduction model. For heat conduction problem, the dispersion characters of the formulation is analyzed through spectral approach and the truncation error is studied by Taylor expansion of the discretized governing equation. It will be shown that the state-based TM PD formulation may experience amplified numerical oscillation and errors owing to its non-local nature. As a strategy of remedy, a novel multi-horizon

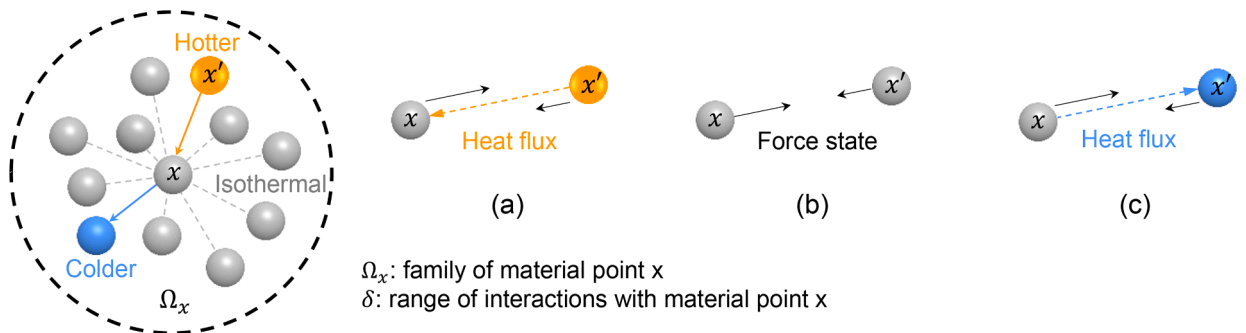


Fig. 1. Schematics of thermomechanical state-based PD. Shown in the figure are interactions between the master material point and (a) hotter material point (force state and heat flux form  $x'$  to  $x$ ); (b) isothermal material point (force state only); (c) colder material point (force state and heat flux from  $x$  to  $x'$ ).

computational scheme is introduced for the coupled thermo-mechanical PD model. It is demonstrated that the multi-horizon scheme offers appreciable improvements in the simulation accuracy.

This paper is organized as follows. In Section 2, we present a new fully coupled thermomechanical state-based PD model, including a temperature-dependent constitutive model and a heat conduction model with consideration of the effects of deformation on temperature. In Section 3, the dispersion relation and error analyses of PD heat equation are investigated from a mathematical perspective. Section 4 presents the principles and algorithm of a multi-horizon scheme for coupled thermo-mechanical modeling. Multiple numerical examples are provided for validation purpose in Section 5, including heat conduction model, coupled thermo-mechanical models, and thermal fracturing model. Finally, conclusion and a discussion on the proposed computational scheme are given in Section 6.

## 2. Fully coupled thermomechanical state-based peridynamics

In the PD theory, a continual media is modeled by discretized material points. The material points interact with each other within a certain distance range, as illustrated in Fig. 1. This range is denoted by  $\delta$  and is named *horizon*. The set of material points within the horizon of  $\mathbf{x}$  is termed *family* of  $\mathbf{x}$  and is denoted by  $\Omega_x$ . Under non-isothermal conditions, the interactions between material points involve not only the mechanical response but also the heat transfer process. As illustrated in Fig. 1, when a master point,  $\mathbf{x}$ , has a hotter neighboring point,  $\mathbf{x}'$ , the bond force applies along with the heat flow from  $\mathbf{x}'$  to  $\mathbf{x}$ . On the contrary, when the master point,  $\mathbf{x}$ , is colder than a neighboring point,  $\mathbf{x}'$ , the heat flows from  $\mathbf{x}$  to  $\mathbf{x}'$ . The material response is determined by the coupled thermal and mechanical fields. In other words, the total force acting on material point  $\mathbf{x}$  consists of a structural force component, which follows the constitutive law of the material under isothermal condition, and a thermal component which originates from the temperature change. Meanwhile, the temperature of material point  $\mathbf{x}$  is determined by the collective heat flux of neighboring points as well as the deformation of those neighbors. The key of developing a fully coupled thermomechanical PD model involves a temperature-dependent constitutive model and a deformation-dependent heat conduction model. The two key aspects are addressed in Sections 2.1 and 2.2. The formulations are derived for the state-based PD.

### 2.1. Temperature-dependent constitutive model

The general form of the equation of motion in the state-based PD can be expressed by

$$\rho(\mathbf{x})\ddot{\mathbf{u}}(\mathbf{x}, t) = \int_{\Omega_x} [\mathbf{T} \langle \mathbf{x}' - \mathbf{x} \rangle - \mathbf{T} \langle \mathbf{x} - \mathbf{x}' \rangle] dV_{x'} + \mathbf{b}(\mathbf{x}) \quad (1)$$

where  $\rho$  represents density at a material point,  $\mathbf{u}$  represents material point deformation,  $\mathbf{b}$  represents body force density and  $V_{x'}$  denotes the volume of a neighbor point  $\mathbf{x}'$ .  $\mathbf{T} \langle \mathbf{x}' - \mathbf{x} \rangle$  is a *force state* which represents the force exerted by  $\mathbf{x}'$  on  $\mathbf{x}$  and the angle bracket represents the bond that the state operates on. Note that if  $\mathbf{T} \langle \mathbf{x}' - \mathbf{x} \rangle$  equals  $\mathbf{T} \langle \mathbf{x} - \mathbf{x}' \rangle$ , the state-based PD reduces to the bond-based PD. The force state maps the deformation of a bond into a force vector and different constitutive models can be implemented in the calculation of the force state. For an ordinary material, the force state act on the bond  $\boldsymbol{\xi} = \mathbf{x}' - \mathbf{x}$  is computed by (Silling et al., 2007)

$$\mathbf{T} \langle \mathbf{x}' - \mathbf{x} \rangle = t \frac{\mathbf{Y}}{\|\mathbf{Y}\|} \quad (2)$$

where  $t$  represents a scalar force state and  $\mathbf{Y}$  is the deformed bond vector. It is assumed that Eq. (2) remains applicable under non-isothermal conditions, and therefore the key of developing a thermomechanical PD solid model comes to determine the expression of  $t$  under different temperatures. The derivation of  $t$  for the bond-based PD is available in previous work (Oterkus et al., 2014a) and the present study is focused on deriving  $t$  that fits into the state-based PD.

For an elastic material, the scalar force state  $t$  can be obtained by taking the Fréchet derivative of energy density function  $W$  with respect to the extension state  $\underline{e}$  as  $t = \nabla_{\underline{e}} W$ . The term  $\nabla_{\underline{e}} W$  is defined as (Silling et al., 2007)

$$W(\underline{e} + \Delta \underline{e}) = W(\underline{e}) + \nabla_{\underline{e}} W \cdot \Delta \underline{e} + o(\|\Delta \underline{e}\|) \quad (3)$$

in which  $\underline{e}$  can be calculated by  $\|\mathbf{Y}\| - \|\boldsymbol{\xi}\|$ ;  $\Delta \underline{e}$  represents an increment in the extension state;  $o(\|\Delta \underline{e}\|)$  is the residual error. Note that the non-local energy density function  $W_{PD}$  in PD form should be equivalent to classical local energy density function  $W$  (Le et al., 2014), which can be readily obtained from the definition  $W = \int \sigma_{ij} d\varepsilon_{ij}$  and the generalized Hooke's law (Wang, 2017; Zhang and Qiao, 2018, 2020) as

$$W = \begin{cases} G \sum_{ij=1,2,3} \varepsilon_{ij} \varepsilon_{ij} + \frac{\lambda}{2} \left( \frac{dV}{V} \right)^2 - 3k\beta\Delta\Theta \left( \frac{dV}{V} \right) + f(\Theta) & , 3D \\ G \sum_{ij=1,2} \varepsilon_{ij} \varepsilon_{ij} + \left[ G \left( \frac{\nu}{1-\nu} \right)^2 + \frac{\lambda}{2} \left( \frac{1-2\nu}{1-\nu} \right)^2 \right] \left( \frac{dS}{S} \right)^2 - 3k\beta\Delta\Theta \frac{1-2\nu}{1-\nu} \frac{dS}{S} + f(\Theta) & , \text{plane strain} \\ G \sum_{ij=1,2} \varepsilon_{ij} \varepsilon_{ij} + \frac{\lambda}{2} \left( \frac{dS}{S} \right)^2 - 3k\beta\Delta\Theta \frac{dS}{S} + f(\Theta) & , \text{plane strain} \end{cases} \quad (4)$$

where  $G$  and  $k$  are shear and bulk moduli, respectively;  $\lambda$  is lame constant and  $\nu$  is Poisson's ratio;  $\sigma_{ij}$  and  $\varepsilon_{ij}$  are stress tensor and strain tensor, respectively;  $dV/V$  and  $dS/S$  represent volumetric strain and plane strain, respectively;  $\beta$  is the linear coefficient of thermal expansion;  $\Delta\Theta$  denotes the temperature change between the current state and a reference state;  $f(\Theta)$  is a potential energy function associated only with current temperature, which is independent of the stress state.

The non-local peridynamic form of elastic energy density function should converge to the classical local density function when the horizon reduces to zero, by making an analogy between the two (Zhang and Qiao, 2020), one can obtain the peridynamic form energy density function as

$$W_{PD} = \begin{cases} \frac{k}{2} \theta^2 + \frac{15G}{2m} \left( w(\|\xi\|) \underline{e}^d \right) \cdot \underline{e}^d - 3k\beta\Delta\Theta\theta + f(\Theta) & , 3D \\ \frac{1}{2} k' \theta_s^2 + \frac{4G}{m} \left( w(\|\xi\|) \underline{e}^d \right) \cdot \underline{e}^d - 2k'\beta\Delta\Theta\theta_s + f(\Theta) & , \text{plane stress} \\ \frac{1}{2} k' \theta_s^2 + \frac{4G}{m} \left( w(\|\xi\|) \underline{e}^d \right) \cdot \underline{e}^d - 2k'(1+\nu)\beta\Delta\Theta\theta_s + f(\Theta) & , \text{plane strain} \end{cases} \quad (5)$$

where  $\underline{e}^d$  represents the deviatoric part of extension state, which can be calculated by  $\underline{e} - \underline{e}^i$ ;  $\underline{e}^i$  represents the isotropic part of extension state and can be related to dilation  $\theta$  and plane dilation  $\theta_s$  through

$$\underline{e}^i = \begin{cases} \frac{\theta}{3} \|\xi\| & (3D) \\ \frac{\theta_s}{2} \|\xi\| & (2D) \end{cases} \quad (6)$$

the weight volume  $m$ , dilation  $\theta$  (for 3D) and plane dilation  $\theta_s$  (for 2D) are calculated by

$$m = \int_{\Omega_x} w(\|\xi\|) \|\xi\|^2 dV_x \quad (7)$$

$$\theta = \frac{3}{m} \int_{\Omega_x} w(\|\xi\|) \|\xi\| \underline{e} dV_x \quad (8)$$

$$\theta_s = \frac{2}{m} \int_{\Omega_x} w(\|\xi\|) \|\xi\| \underline{e} dV_x \quad (9)$$

Here  $w(\|\xi\|)$  is the weight function that measures the influence of neighboring points. It is chosen to be the Gaussian function in the form of  $w(\|\xi\|) = e^{-\left(\frac{\|\xi\|}{\alpha\delta}\right)^2}$  where the parameter  $\alpha$  is selected to be 0.5. For 2D cases,  $k'$  is defined as the plane bulk modulus and can be calculated based on the Young's modulus  $E$  and Poisson's ratio ( $\nu$ ) by

$$k' = \begin{cases} \frac{E}{2(1-\nu)} & , \text{plane stress} \\ \frac{E}{2(1+\nu)(1-2\nu)} & , \text{plane strain} \end{cases} \quad (10)$$

Substituting the non-local elastic strain energy density  $W_{PD}$  into Eq. (3) yields the scalar force state in the form of

$$t = \begin{cases} \frac{3k}{m}(\theta - 3\beta\Delta\Theta)w\langle \|\xi\| \rangle \|\xi\| + \frac{15G}{m}w\langle \|\xi\| \rangle e^d & , \text{ 3D} \\ \frac{2k'}{m}(\theta_s - 2\beta\Delta\Theta)w\langle \|\xi\| \rangle \|\xi\| + \frac{8G}{m}w\langle \|\xi\| \rangle e^d & , \text{ plane stress} \\ \frac{2k'}{m}[\theta_s - 2(1+\nu)\beta\Delta\Theta]w\langle \|\xi\| \rangle \|\xi\| + \frac{8G}{m}w\langle \|\xi\| \rangle e^d & , \text{ plane strain} \end{cases} \quad (11)$$

It can be noted that the first term in the scalar force state represents a volumetric term due to dilation and temperature change whereas the last term represents a force originated from the deviatoric bond extension.

### 2.2. Deformation-dependent heat conduction model

The general form of the fully coupled peridynamic heat equation writes (Oterkus et al., 2014a)

$$\rho c \frac{D\Theta}{Dt} = \int_{\Omega_x} [\mathbf{h}\langle \mathbf{x}' - \mathbf{x} \rangle - \mathbf{h}\langle \mathbf{x} - \mathbf{x}' \rangle + \Theta \mathbf{B}\langle \mathbf{x}' - \mathbf{x} \rangle \cdot \dot{\mathbf{Y}}\langle \mathbf{x}' - \mathbf{x} \rangle] dV_{x'} + \rho \Theta_b \quad (12)$$

in which  $\rho$  is the density;  $c$  is the specific heat capacity;  $\Theta$  and  $\Theta_b$  represent the absolute temperature and the volumetric heat generation per unit mass, respectively;  $\mathbf{h}\langle \mathbf{x}' - \mathbf{x} \rangle$  denotes the heat flux state;  $\mathbf{B}\langle \mathbf{x}' - \mathbf{x} \rangle$  represents the thermal modulus state and  $\dot{\mathbf{Y}}\langle \mathbf{x}' - \mathbf{x} \rangle$  represents by rate of change of extension. The product of these two terms gives the effect of deformation on temperature. However, in the previous studies, both the heat flow state and the heat flux state are determined for the bond-based PD only. In the present study, we derive a more comprehensive form of the heat equation for the state-based PD by transforming the classical heat equation and Fourier's law using a non-local differential operator.

For heat conduction problems, the continuity equation in its local form is expressed by

$$\rho c \frac{D\Theta}{Dt} = -\nabla \cdot \mathbf{q} + \rho \Theta_b \quad (13)$$

where  $\mathbf{q}$  is the heat flux and can be related to temperature by the Fourier's law as

$$\mathbf{q} = -k_h \nabla \otimes \Theta \quad (14)$$

where  $k_h$  represents the heat conductivity. To derive the heat conduction equation in peridynamic form, we utilize the non-local operators which was introduced in PD to approximate differentiation through integration. Successful attempts on non-local operators have been made to achieve this conversion between derivatives and integrals by Taylor expansion such as Madenci et al., (2019), Rabczuk et al., (2019) and Ren et al. (2020b, 2020a). In this paper, the non-local gradient operator and divergence operator proposed by Bergel and Li (2016) are adopted as

$$\nabla \otimes \mathbf{A} = \left[ \int_{\Omega_x} w\langle \|\xi\| \rangle (\Delta \cdot \mathbf{A}) \otimes \xi dV_{x'} \right] \mathbf{M}_x^{-1} \quad (15)$$

$$\nabla \cdot \mathbf{A} = \int_{\Omega_x} w\langle \|\xi\| \rangle (\Delta \cdot \mathbf{A}) \cdot (\mathbf{M}_x^{-T} \xi) dV_{x'} \quad (16)$$

where  $\mathbf{A}$  is a vector field and  $\Delta \cdot \mathbf{A} = \mathbf{A}_{x'} - \mathbf{A}_x$  is defined as the non-local difference operator; the shape tensor  $\mathbf{M}_x$  is calculated as

$$\mathbf{M}_x = \int_{\Omega_x} w\langle \|\xi\| \rangle \xi \otimes \xi dV_{x'} \quad (17)$$

Note that even if  $\mathbf{A}$  reduces to a scalar, such as temperature in Eq. (14), the abovementioned operators remain applicable. The above non-local operator has been proven to converge to the local gradient and divergence operators when the horizon approaches zero (Tu and Li, 2017). Substituting Eqs. (15)-(16) into Eqs. (13)-(14) yields the non-local heat equation and Fourier's law

$$\rho c \frac{D\Theta}{Dt} = \int_{\Omega_x} w\langle \|\xi\| \rangle (\mathbf{q}_x \mathbf{M}_x^{-T} \xi\langle \mathbf{x}' - \mathbf{x} \rangle - \mathbf{q}_x \mathbf{M}_x^{-T} \xi\langle \mathbf{x} - \mathbf{x}' \rangle) dV_{x'} + \rho \Theta_b \quad (18)$$

$$\mathbf{q}_x = -k_h \left[ \int_{\Omega_x} w\langle \|\xi\| \rangle \Theta\langle \mathbf{x}' - \mathbf{x} \rangle \xi dV_{x'} \right] \mathbf{M}_x^{-1} \quad (19)$$

where the temperature state is defined as

$$\Theta(\mathbf{x}' - \mathbf{x}) = \Theta_{\mathbf{x}'} - \Theta_{\mathbf{x}} \quad (20)$$

The Eqs. (18) and (19) are implemented in the state-based PD. Note that the classical heat conductivity  $k_h$  is directly used in the state-based PD formulation. This eliminates the need of finding a micro-conductivity value in bond-based PD. However, the local heat equation given in Eq. (13) does not consider the possible temperature variation induced by deformation. To consider such effect, an additional term has been added into Eq. (18) and the fully coupled heat conduction equation take the form of

$$\rho c \frac{D\Theta}{Dt} = \int_{\Omega_x} [w(\|\xi\|) (\mathbf{q}_x \mathbf{M}_x^{-T} + \mathbf{q}_x \mathbf{M}_x^{-T}) \xi + \Theta \mathbf{B}(\mathbf{x}' - \mathbf{x}) \cdot \dot{\mathbf{Y}}(\mathbf{x}' - \mathbf{x})] dV_{x'} + \rho \Theta_b \quad (21)$$

where the thermal modulus state  $\mathbf{B}(\mathbf{x}' - \mathbf{x})$  can be determined by referencing to the force state given in Eq. (11) given that the thermal effect on the force state should be represented by  $\mathbf{B}(\mathbf{x}' - \mathbf{x}) \Delta \Theta$

$$\mathbf{B}(\mathbf{x}' - \mathbf{x}) = \begin{cases} \frac{3k}{m} \beta w(\|\xi\|) \|\xi\| \|\xi\| \frac{\mathbf{Y}}{\|\mathbf{Y}\|} & , 3D \\ \frac{4k'}{m} \beta w(\|\xi\|) \|\xi\| \|\xi\| \frac{\mathbf{Y}}{\|\mathbf{Y}\|} & , \text{plane stress} \\ \frac{4k'(1+\nu)}{m} \beta w(\|\xi\|) \|\xi\| \|\xi\| \frac{\mathbf{Y}}{\|\mathbf{Y}\|} & , \text{plane strain} \end{cases} \quad (22)$$

**Remark 1.** The effect of deformation on temperature variation may be negligible for typical brittle-elastic materials owing to the small deformation before fracturing. However, such effect is more pronounced when a material undergoes plastic deformation. An example refers to growing fracture in metals where a plastic region forms ahead of the crack tip which leads to temperature increase with the dissipation of mechanical energy. Nevertheless, when dealing with plastic material responses with large deformations, it is essential to conduct a careful investigation to determine if the current total-Lagrangian scheme remains applicable and appropriate.

### 2.3. Damage model

In peridynamics, the fracture of solid is modeled by the breakage of bonds between material points. A common approach to determine bond breakage under mechanical loads is through the critical stretch model (Silling and Askari, 2005), which states that a bond breaks irreversibly when it exceeds a predefined limit of strain. This critical stretch for bond failure can be expressed as

$$s_c = \sqrt{\frac{5G_c}{9K\delta}} \quad (23)$$

where  $G_c$  denotes the critical energy release rate. The local damage of a material point can be calculated by averaging the failure at bond level

$$\varphi = 1 - \frac{\int_{\Omega_x} g(\xi) dV_{x'}}{\int_{\Omega_x} dV_{x'}} \quad (24)$$

in which  $g(\xi)$  is a binary scalar-valued function that takes the value of either 1 (for intact bond) or 0 (for broken bond).

In the case of thermally induced fracturing, opening of fractures on the free surface, away from the heat source, is predominantly attributed to the tensile stress (and subsequently thermal expansion) induced by temperature change. Our experience shows that the performance of the critical stretch model in such scenario is less satisfactory than expected. A possible reason is that the critical stretch value is dependent of the weight function, using a weight function different from the one for derivation of Eq. (23) can potentially induce inaccuracies. Also, since different horizons are used for the thermal and mechanical fields (as will be introduced in later sections), the critical stretch of bonds, which is assessed with the horizon of the mechanical field, may deviate from the length scale that is used for thermal field modeling. Therefore, in this study, an additional tensile stress-based failure model is implemented alongside the critical stretch model. With this model, a material point fails when its major principal stress exceeds the tensile strength of the material. Therefore, the local damage of a material point can reach 1.0 under two circumstances: a) bonds between all interacting materials break; and b) major principal stress exceeds the material's tensile strength.

### 3. Peridynamic thermal wave dispersion and error analysis

It is well known that the non-locality of peridynamics brings wave dispersion in transient analysis. The dispersive response of both bond-based and state-based PD in modeling elastic wave propagation has been extensively investigated based on the spectral approach (Bazant et al., 2016; Butt et al., 2017; Gu et al., 2016; Kulkarni and Tabarraei, 2018; Mikata, 2012; Silling, 2016; Wang et al., 2022a). It was found that both the non-local nature of PD and the discretization introduce dispersion. Furthermore, the dispersion depends on a variety of model settings including horizon, weight function and material point size. In general, larger horizon and coarser mesh are

associated with stronger dispersion, while the state-based formulation is more dispersive than the bond-based formulation (Bažant et al., 2016).

The heat conduction is a dissipative process, which tends to dampen and smoothen out the waveforms over time. Moreover, thermal waves can exist when variations or fluctuations in temperature propagates through a medium. For example, in the case of periodic heating or cooling (e.g., in laser-induced heating or pulsed heating experiments), thermal waves can be generated. These thermal waves exhibit wave-like behaviors such as dissipation and dispersion just like other types of waves. When modeling heat conduction processes by PD, due to the non-local feature of the method, heat transfer is modeled not only between adjacent neighboring points but also between points that are not immediate neighbors. That is, the heat transfer may skip some intermediate material points lying between the paired points of a bond. This is true from an atomic perspective, which however does not hold at macro- or meso-scale where PD is generally applied. Therefore, it is essential to further examine the dispersion relation and numerical errors of the non-local PD heat equation, which will offer insights into the non-local effect on the accuracy of the numerical solution and facilitate finding possible remedies. To the best knowledge of the authors, the study on thermal wave dispersion properties of the state-based PD has not been done in past studies.

### 3.1. Dispersion relation

In this section, we analyze dispersion relations for heat conduction in state-based peridynamic continua. Since the 2D and 3D analyses are similar to 1D case, only the detailed derivations of 1D case are presented here for clarity. To obtain the dispersion relation, a periodic thermal wave at material point  $x$  and time  $t$  is introduced as

$$\Theta(x, t) = A e^{i(kx - \omega t)} \quad (25)$$

in which  $A$  is the amplitude of the wave (the maximum temperature from the equilibrium state);  $k$  and  $\omega$  denote the wave number and angular frequency, respectively;  $i$  represents the imaginary unit. Note that it is enough to analyze harmonic temperature variations, since any periodic wave or non-periodic wave can be expanded into Fourier series or Fourier transform, respectively.

Considering the heat conduction in an infinite 1D elastic state-based peridynamic continuum, the non-local governing equation becomes (neglecting the body heat generation and heat generated by deformation)

$$\rho c \frac{D\Theta}{Dt} = \int_{-\delta}^{\delta} w(\xi) (q_x M_x^{-T} + q_x M_x^{-T}) \xi d\xi \quad (26)$$

where the bond length  $\xi = x' - x$  becomes a scalar value. Assume a unity weight function for convenience, the shape tensor also degenerates to a scalar value and is the same at all points (except at the boundary) for the 1D case

$$M_x = M_{x'} = \int_{-\delta}^{\delta} w(\xi) \xi^2 d\xi = \frac{2\delta^3}{3} \quad (27)$$

According to Eq. (19), the heat flux at two different material points  $x$  and  $x'$  are given as

$$q_x = -k_h \frac{\int_{-\delta}^{\delta} (\Theta_{x+\xi} - \Theta_x) \xi d\xi}{\int_{-\delta}^{\delta} w(\xi) \xi^2 d\xi} \quad (28)$$

$$q_{x'} = -k_h \frac{\int_{-\delta}^{\delta} (\Theta_{x'+\eta} - \Theta_{x'}) \eta d\eta}{\int_{-\delta}^{\delta} w(\eta) \eta^2 d\eta} \quad (29)$$

Substituting the periodic thermal cycling given in Eq. (25) into Eqs. (28)-(29) and Eq. (26), one can obtain

$$-\rho c \omega i = \frac{9k_h}{4\delta^6} \int_{-\delta}^{\delta} \left[ \int_{-\delta}^{\delta} (e^{ik\xi} - 1) \xi d\xi + \int_{-\delta}^{\delta} e^{ik\xi} (e^{ik\eta} - 1) \eta d\eta \right] \xi d\xi \quad (30)$$

This equation can be further simplified by using the Euler formula and the symmetric property of material points within horizon into the form of

$$-\rho c \omega i = \frac{9k_h}{4\delta^6} \int_{-\delta}^{\delta} \left[ \int_{-\delta}^{\delta} i\xi \sin(k\xi) d\xi + e^{ik\xi} \int_{-\delta}^{\delta} i\eta \sin(k\eta) d\eta \right] \xi d\xi \quad (31)$$

By calculating the integrals in Eq. (31), we obtain the 1D dispersion relation of PD heat equation in terms of angular frequency

$$\omega = -i \frac{9k_h}{\rho c} \left[ \frac{\sin(k\delta) - \delta k \cos(k\delta)}{k^2 \delta^3} \right]^2 \quad (32)$$

The imaginary solution obtained in Eq. (32) represents the dissipative nature of heat conduction. This can be demonstrated by substituting Eq. (32) into Eq. (25). By doing so, one can derive the expression  $\Theta(x, t) = Ae^{ikx}e^{-|\omega|t}$ , in which  $Ae^{ikx}$  represents the initial wave shape and the length of  $\omega$  indicates the damping rate of thermal wave. This indicates that solving heat equation by PD non-local operators will not induce extra dispersion and will not violate the nature of heat conduction. However, the dispersion relation of PD heat equation is clearly different from the local analytical solution ( $\omega = -ik_n k^2 / \rho c$ ). A quantitative comparison is presented between the results of local methods and PD for the normalized angular frequency ( $\omega_n = \omega / -i$ ) plotted against the square of the wave number in Fig. 2. It can be found that the numerical results converge to the local analytical solution as horizon approaches zero. Moreover, the dissipative rate of PD heat equation becomes smaller as the horizon increases, especially for waves with high frequency and short wavelength. This means the magnitude of thermal wave dampens slower when adopting larger horizon. The mathematical findings for state-based PD in this study are consistent with the parametric analyses conducted by Agwai (2011) for bond-based PD, in which a heated bar with zero temperature boundary is modeled. In Section 3.3, we will also conduct a benchmark for 1D heat conduction problem to showcase the effects of horizon within the state-based PD framework.

**Remark 2.** The state-based PD heat equation does not alter the inherent non-dispersive nature of the heat conduction process; however, it significantly reduces the dissipation rate of thermal waves, i.e., a slower heat conduction process, with increasing horizon.

### 3.2. Truncation error of discretized PD heat equation

It is widely recognized in the FEM and finite difference method (FDM) that, despite of using non-dispersive governing equations, the discretization process itself can introduce additional dispersion (Bažant et al., 2016; Butt et al., 2017). Discretization generates inherent non-local properties because mass is lumped at discrete elements or points. It is a natural assumption to expect that the error introduced by discretization can be eliminated when the mesh is refined sufficiently, such as reaching the atomic size scale. Unfortunately, achieving a material point size that fine is computationally unfeasible due to the prohibitively high computational cost it would entail. Like FEM and FDM, the PD heat equation is not exempt from errors arising from discretization. In this section, a comprehensive analysis is performed to identify and examine the sources of error in the PD heat equation. The objective is to provide insights and guidance on minimizing these errors beyond simply refining the mesh.

Consider the discretized form of 1D PD heat equation, where forward difference is utilized to approximate the temporal derivative and the horizon is meshed into  $(J + 1)$  discretized material points

$$\rho c \frac{\Theta_i^{n+1} - \Theta_i^n}{\Delta t} = \sum_j^J w(\xi) (q_l M_l^{-T} + q_j M_j^{-T}) \xi \tag{33}$$

where  $\Theta_i^n$  represents the temperature of material point  $i$  at step  $n$ ;  $j$  denotes a neighboring material of master material point  $i$ ; the discretized heat flux formula of material point  $i$  and  $j$  are given as

$$q_i = -k_h \left[ \sum_j^J w(\xi) (\Theta_j - \Theta_i) \xi_{ij} \right] M_i^{-1} \tag{34}$$

$$q_j = -k_h \left[ \sum_l^J w(\xi) (\Theta_l - \Theta_j) \xi_{jl} \right] M_j^{-1} \tag{35}$$

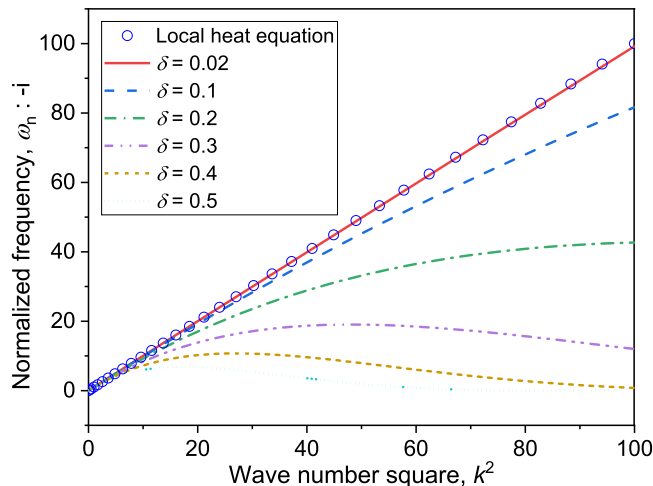


Fig. 2. Relation between normalized angular frequency and wave number for state-based PD heat equation.

in which the discretized shape tensor of material point  $i$  and  $j$ ,  $M_i$  and  $M_j$ , can be calculated by

$$M_i = \sum_j^J w(\xi) \xi_{ij}^2 \tag{36}$$

$$M_j = \sum_l^J w(\xi) \xi_{jl}^2 \tag{37}$$

Let  $\Theta(i, n)$  be the exact solution to the PD heat equation, the following equation holds according to Eq. (26)

$$\rho c \frac{\partial \Theta(i, n)}{\partial t} = \sum_j^J w(\xi) \left[ -k_h \frac{\partial \Theta(i, n)}{\partial x} M_i^{-T} - k_h \frac{\partial \Theta(j, n)}{\partial x} M_j^{-T} \right] \xi \tag{38}$$

We can further express  $\Theta(j, n)$  and  $\Theta(i, n+1)$  by the exact solution  $\Theta(i, n)$  based on the Taylor expansion

$$\Theta(j, n) = \Theta(i, n) + \frac{\partial \Theta(i, n)}{\partial x} \xi_{ij} + \frac{1}{2!} \frac{\partial^2 \Theta(i, n)}{\partial x^2} \xi_{ij}^2 + \frac{1}{3!} \frac{\partial^3 \Theta(i, n)}{\partial x^3} \xi_{ij}^3 \dots \tag{39}$$

$$\Theta(i, n+1) = \Theta(i, n) + \frac{\partial \Theta(i, n)}{\partial t} \Delta t + \frac{1}{2!} \frac{\partial^2 \Theta(i, n)}{\partial t^2} (\Delta t)^2 + \dots \tag{40}$$

Substituting Eqs. (38)–(40) into Eqs. (33)–(35), the truncation error  $T_i^n$  of PD heat equation takes the following form (omitting the spatial terms higher than third order and the temporal terms higher than second order)

$$T_i^n = \rho c \left[ \frac{1}{2} \frac{\partial^2 \Theta(i, n)}{\partial x^2} \Delta t \right] + \frac{k_h}{6} \sum_j^J w(\xi_{ij}) \left[ M_i^{-T} \frac{\partial^3 \Theta(i, n)}{\partial x^3} \frac{\sum_l^J w(\xi_{il}) \xi_{il}^4}{M_i} + M_j^{-T} \frac{\partial^3 \Theta(j, n)}{\partial x^3} \frac{\sum_l^J w(\xi_{jl}) \xi_{jl}^4}{M_j} \right] \xi_{ij} \tag{41}$$

The discretized scheme is of one-order accuracy in time and two-order accuracy in space if the weight function is linearly related to the bond length. Only one-order accuracy in space is achieved if the unity weight function is employed as will be proven in Eq. (43). One can certainly employ other higher order integration scheme to achieve higher order accuracy, while it is out of the scope of this paper since the current scheme is already consistent because the truncation error approaches zero as  $\Delta t$  and  $\xi_{ij}$  approaches zero. We want to pay special attention to the effects of horizon and material point size on the error. Assume a uniform discretization in space leads to  $|\xi_{ij}| = m\Delta x$ , where  $m$  represents the  $m$ -th material point away from master material point as shown in Fig. 3. The shape tensor and truncation error can be rewritten as

$$M_i = M_j = \sum_{m=1}^L 2m^2 (\Delta x)^2 = \frac{L(L+1)(2L+1)}{3} (\Delta x)^2 \tag{42}$$

$$T_i^n = \frac{k_h}{10} \frac{3L^2 + 3L - 1}{L(L+1)(2L+1)} \sum_{m=1}^L \left[ \frac{\partial^3 \Theta(m^+, n)}{\partial x^3} - \frac{\partial^3 \Theta(m^-, n)}{\partial x^3} \right] m \Delta x \tag{43}$$

in which we use unity weight function again here for convenience;  $L = J/2$ . Note that the symmetric property of the material points within horizon is used several times when deriving Eq. (41) and Eq. (43).

According to Eq. (43), the truncation error is dependent on both the material point size and the number of neighboring material points, i.e., horizon size. It is clear that the error diminishes as the material point size approaches zero, while it is not so straightforward to draw a conclusion with respect to horizon. But it is also not hard to prove that the  $L$ -associated term in Eq. (43) is a monotonically

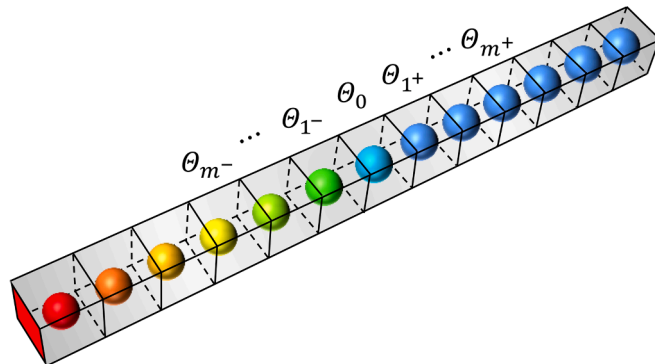


Fig. 3. Discretized PD heat equation for 1D rod

increasing function. Therefore, qualitatively, larger horizon yields more deviations from the analytical solution. In the following section, we will conduct quantitative parametric analyses on the effects of horizon and material point size.

3.3. Comparisons between PD and analytical solutions for 1D heat conduction problem

Consider an infinite 1D bar with parameters given as  $\rho = 1 \text{ kg/m}^3$ ,  $c = 1 \text{ J/kg}^\circ\text{C}$  and  $k_h = 1 \text{ W/m}^\circ\text{C}$ . The initial temperature of the bar  $\Theta_0$  is set to be  $0^\circ\text{C}$  and constant temperature  $\Theta_1 = 100^\circ\text{C}$  is applied on one side of the bar as shown in Fig. 3. The analytical solution of this problem is given as (Hahn and Özisik, 2012)

$$\Theta(x, t) = \text{erfc}\left(\frac{x}{2\sqrt{\frac{k_h}{\rho c} t}}\right) (\Theta_1 - \Theta_0) + \Theta_0 \tag{44}$$

With a uniform mesh and a material point size of 0.02 m, numerical solution is obtained for the temporal variation of temperature at a material point located one meter away from the heat boundary. Simulations are performed with varied horizon size and the results are presented in Fig. 4 with comparison to the analytical solution. Evidently, only the numerical results from  $\delta = \Delta x$  match well with the analytical solution, while the temperature become much lower than the analytical solution as horizon increases. This can be well explained by Eq. (32) and Fig. 2, where a lower dissipation rate is associated with a larger horizon. The discrepancy between PD and analytical solutions increases nearly exponentially with the horizon size, which is also consistent with the mathematical formulation in Eq. (32). The relative error of the PD heat equation is further assessed using the relative  $L_1$  loss which is calculated by  $e_1 = (w_a - w_n) / w_a$ , where  $w_a$  and  $w_n$  represent analytical and numerical solution of temperature at each material point, respectively. As shown in Fig. 4(b), the numerical solution of temperature is almost always lower than analytical one due to a smaller dissipation rate of non-local method. Moreover, for  $\delta = 3\Delta x$  and  $\delta = 6\Delta x$ , the numerical results exhibit significant oscillations. The peaks and valleys of these two curves align precisely with the centers of the material points. This phenomenon can be attributed to two factors: (a) the error term described in Eq. (43) increases as the horizon expands, contributing to the larger deviations from analytical solution observed for  $\delta = 6\Delta x$ ; b) for large horizons such as  $\delta = 3\Delta x$  and  $\delta = 6\Delta x$ , the error term exhibits a highly non-local behavior. In other words, non-physical effects, such as the particle-skipping heat flux (i.e., heat flow between a pair of points that jumps intermediate points), are introduced with large non-locality which contribute to the oscillation in the solution. Note that discretized PD equation is similar to high-order FDM in some ways, where more than three points are used to approximate the derivatives in both methods. However, in high-order FDM, it is customary to assign negative coefficients to the non-neighboring points as means to counterbalance the non-locality introduced by their inclusion, whereas the weight function in PD is always positive. From this perspective, using PD with large horizon to model heat conduction process is not recommended. The numerical results for  $\delta = \Delta x$  is clearly noise free and the error is generally within 1 %.

The error in the simulation may also be reduced by refining the mesh as implied by Eq. (43). Its effectiveness is examined and presented in Fig. 5(a) for a fixed horizon  $\delta = 3\Delta x$  with varied material point size. It is found that while the error is reduced, more severe oscillations are presented with finer mesh as the error is associated with the position of each material point. The spatial oscillation of result is undesirable. Hence, merely reducing the material point size may be insufficient in minimizing the error in a PD model of heat conduction. As a comparison, Fig. 5(b) shows the relative error with a smaller horizon of  $\delta = \Delta x$  with different material point size. Clearly, a smaller horizon offers a much smoother solution in space. The results imply that reducing the horizon is more effective and reliable than reducing material point size when minimizing the error in PD heat conduction model.

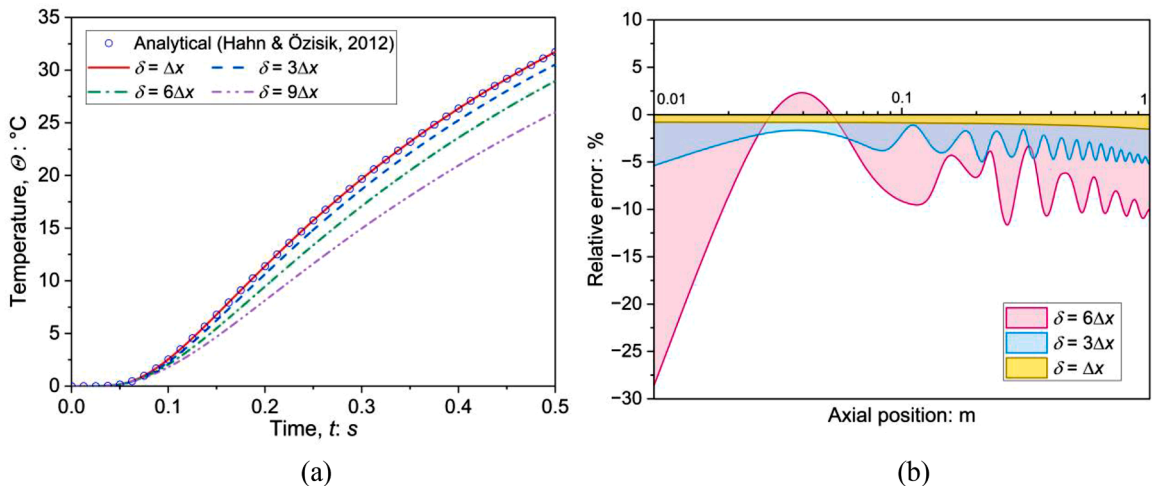


Fig. 4. (a) Comparisons of temperature between analytical solution and PD results with different horizons; and (b) Relative error of PD results.

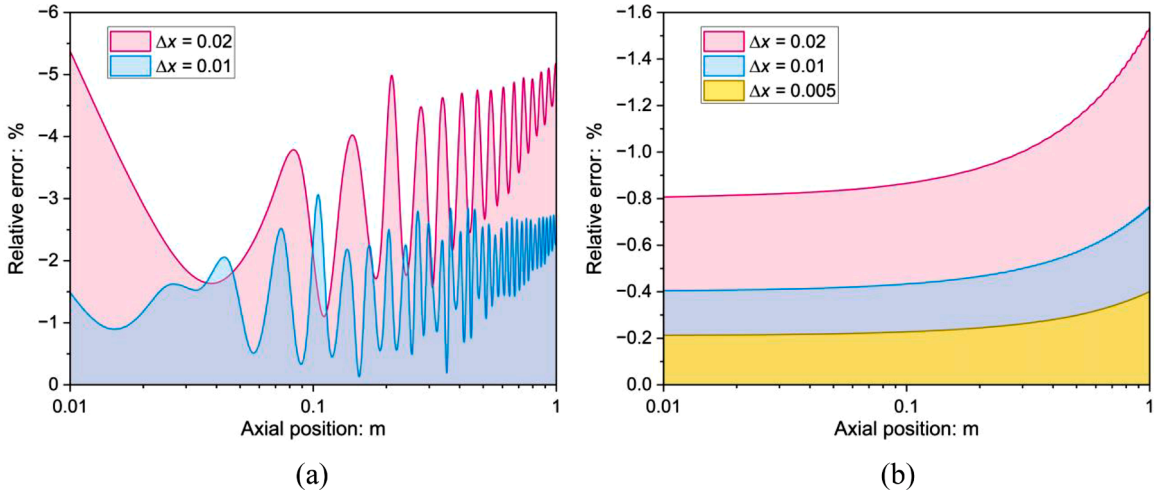


Fig. 5. Relative error of different material point sizes for: (a)  $\delta = 3\Delta x$  and (b)  $\delta = \Delta x$ .

**Remark 3.** The error in the PD heat equation stems from two main sources: (a) the slower heat conduction due to non-locality; and (b) the truncation error introduced by the discretization scheme. Both errors can be mitigated by refining the mesh and reducing the horizon size. However, it is important to note that the noise in the heat equation, specifically related to particle-skipping heat flux, can only be effectively reduced by minimizing the horizon size.

#### 4. Multi-horizon peridynamics for multi-physics coupling

In previous sections, we have showed that when solving the peridynamic heat conduction equation, it is important to adopt an appropriate horizon. A small horizon is effective in mitigating the numerical oscillations and improving the simulation accuracy for heat conduction problem. However, as a typical non-local method, PD is primarily designed to capture non-local effects and long-range interactions in material behavior. This includes crack initiation and propagation where the influence of deformation may extend beyond the immediate vicinity of a material point. In fact, it is necessary to keep the horizon sufficiently large to capture possible crack branching directions in dynamic fracture problems (Ha and Bobaru, 2010). Past studies have also shown that good accuracy can be achieved with the horizon size of  $\delta = 3\Delta x$  (Madenci and Oterkus, 2014; Silling and Askari, 2005) when modeling mechanical material response using PD.

A dilemma arises when developing the coupled thermo-mechanical PD and modeling thermally induced fracturing (e.g., quenching). On one hand, as mentioned earlier, adopting a small horizon may not be effective in capturing possible crack branching in

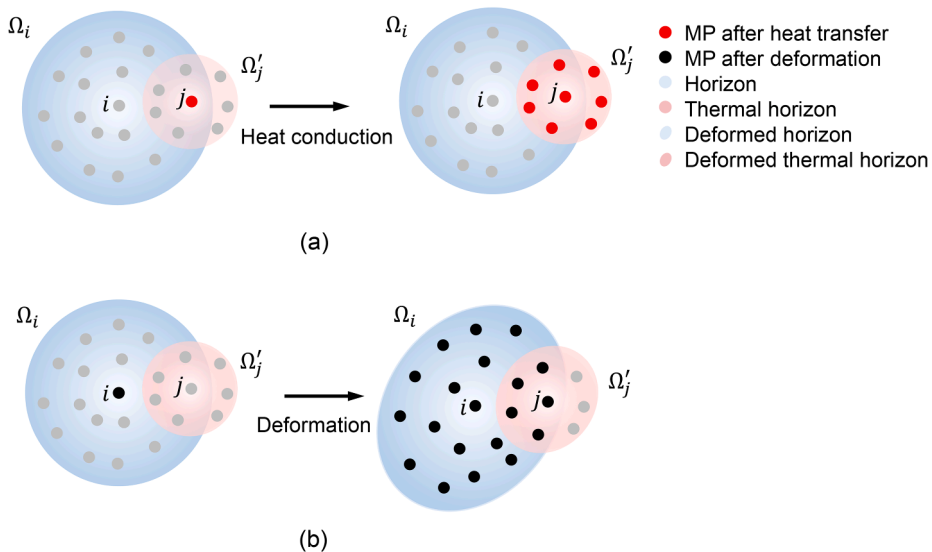


Fig. 6. Schematic of multi-horizon scheme: (a) Heat conduction process of point  $j$ ; and (b) Mechanical response of point  $i$ .

different directions. On the other hand, if a large horizon is adopted, numerical issues such as slower heat conduction rate and oscillating thermal field can be expected. This is especially true for computations near the boundary where obvious numerical oscillations are found for temperature field. The errors in temperature field will induce unphysical thermal expansion or shrinkage which deteriorates the accuracy of the coupled simulation. While the oscillations can be mitigated by numerical means such as smoothing or damping (Chang et al., 2022; Gao and Oterkus, 2020; Monaghan, 1994; Yang et al., 2024), applying those numerical stabilization techniques for heat conduction can lead to an accelerated dissipation rate of thermal energy and is unpreferred herein. A natural solution for the coupled thermo-mechanical PD, as introduced below, is to adopt different horizon sizes for different physics field, to accommodate the distinct characters of the physics fields while maintaining a decent simulation accuracy.

The idea behind multi-horizon PD is straightforward. As shown in Fig. 6, two different horizons are defined. One is the classical horizon  $\delta$  (hereafter referred to as ‘‘horizon’’) to capture the non-local effects in the mechanical field. Another is the thermal horizon  $\delta'$ , which can be defined as a constant smaller than the horizon, used to model the local heat conduction. With the thermal horizon  $\delta'$ , the thermal neighbor list  $\Omega'_x$  is established, and Eqs. (19) and (21) can be recast correspondingly as

$$\mathbf{q}_x = -k_h \left[ \int_{\Omega'_x} w(\|\xi\|) \Theta(\mathbf{x}' - \mathbf{x}) \xi \, dV_{x'} \right] \mathbf{M}_x^{-1} \tag{45}$$

$$\rho c \frac{D\Theta}{Dt} = \int_{\Omega'_x} [w(\|\xi\|) (\mathbf{q}_x \mathbf{M}_x^{-T} + \mathbf{q}_x \mathbf{M}_x^{-T}) \xi + \Theta \mathbf{B}(\mathbf{x}' - \mathbf{x}) \cdot \dot{\mathbf{Y}}(\mathbf{x}' - \mathbf{x})] dV_{x'} + \rho \Theta_b \tag{46}$$

Note that the mechanical field can still be model by the formulations given in Section 2.1 without any modifications.

The heat flux equation Eq. (45) and the heat conduction equation Eq. (46), including the heat generated or dissipated by deformation, are solved within the thermal horizon. However, no kinematical unknowns are updated within thermal horizon even for the thermally induced stress and deformation. This is illustrated in Fig. 6(a), after solving the thermal field, the shapes of both the horizon and the thermal horizon remain unchanged, and the positions of all material points remain unchanged. All the kinematical unknowns (displacement, velocity and acceleration) are calculated and updated within the horizon as illustrated in Fig. 6(b). The effects of temperature variation on deformation are considered herein, and the shape of both horizon and thermal horizon and positions of all material points are updated.

A staggered computational scheme is adopted to solve the fully coupled thermo-mechanical PD equations. Neighbor searching is performed at the beginning of the simulation and two neighbor lists, one based on the horizon and another based on the thermal horizon, are established and used throughout the simulation. For each step of simulation, the flux and temperature are first solved with

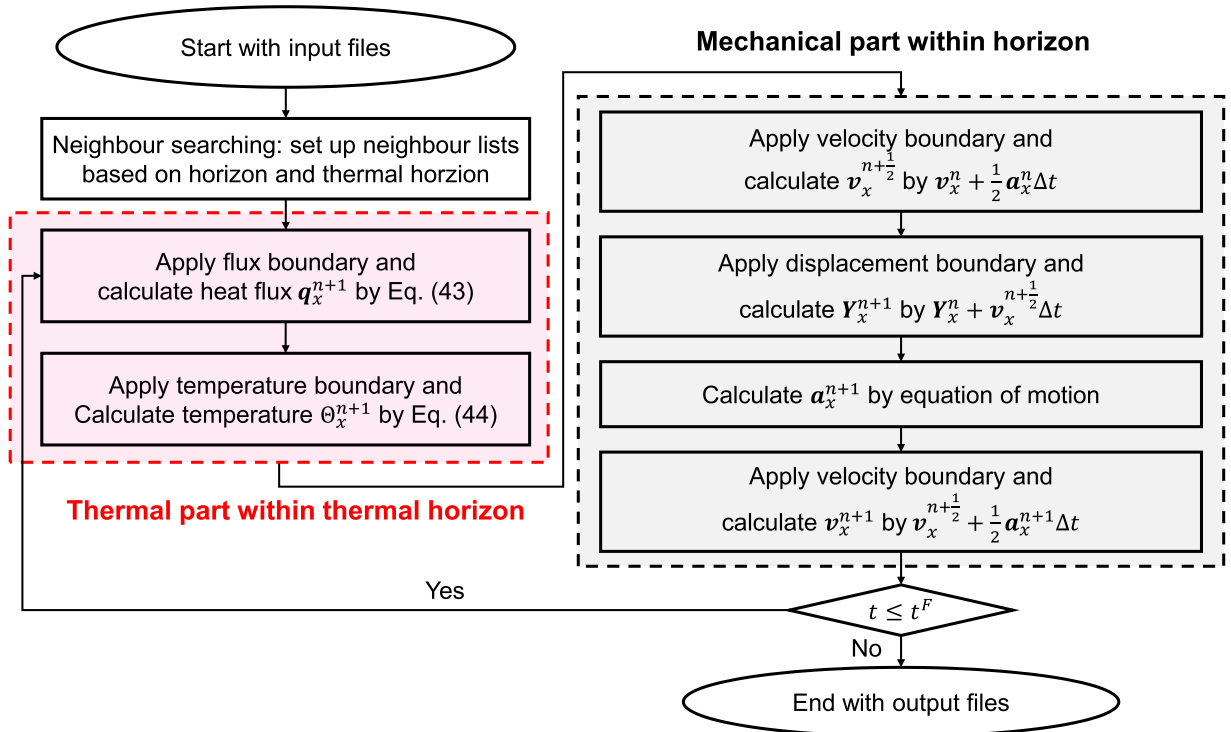


Fig. 7. Flow chart of computation in the multi-horizon PD.

an explicit scheme using forward time difference while other variables remain constant, and the remaining kinematical unknowns are updated with the new temperature using the velocity Verlet scheme. The computational flow chart is shown in Fig. 7.

It should be noted that the proposed multi-horizon PD approach is distinct from the dual-horizon PD introduced by Ren et al., (2016, 2017). The dual-horizon PD incorporates variable horizons at different material points and is suitable for the case where different material point sizes are used. The proposed multi-horizon PD is for simulation of coupled responses across multiple physical fields where a distinct horizon can be selected for each physical field.

## 5. Numerical examples

### 5.1. Thermomechanical response of 2D slab under thermal loading

To benchmark the proposed multi-horizon PD, we first simulate the thermomechanical response of a 2D slab subject to thermal loadings. A 1m by 1m finite slab with both thermal and mechanical boundaries is modeled as shown in Fig. 8. The initial temperature of the slab is set to be 0 °C and constant temperature boundary equal to 1 °C is applied on the bottom and left boundaries of the slab. The displacement of bottom and left boundaries is fixed in y and x directions, respectively. The material parameters used are summarized as follows: density  $\rho = 1 \text{ kg/m}^3$ , Young's modulus  $E = 1 \text{ Pa}$ , Poisson's ratio  $\mu = 0.25$ , linear thermal expansion coefficient  $\beta = 1 \times 10^{-6} \text{ }^\circ\text{C}^{-1}$ , specific heat capacity  $c = 1 \text{ J/(kg}\cdot^\circ\text{C)}$ , thermal conductivity  $k_h = 0.1 \text{ W/(m}\cdot^\circ\text{C)}$ . The material point size is set as 0.01 m, with 10,000 material points for the slab in total. The horizon is taken to be  $\delta = 3\Delta x$ , while the thermal horizon is adopted as  $\delta' = \Delta x$ . Note that applying the temperature boundary requires only one layer of material points with the multi-horizon scheme. This serves as a notable advantage, particularly for large-scale 3D models, as it allows for significant reduction in the number of material points required for the boundary. Since there is no available analytical solution for this particular transient problem, the commercial software COMSOL Multiphysics based on finite element method (FEM) is employed to benchmark the proposed method.

The temperature and displacement distribution in the slab after 0.5s simulation obtained from FEM and multi-horizon PD are shown in Fig. 9. Evidently, the prediction of temperature and displacement distribution by multi-horizon PD is consistent with that by FEM. A further quantitative comparison of the temporal evolutions of temperature and displacement magnitude at point (0.5, 0.5) is shown in Fig. 10. Again, good agreements are observed between FEM and multi-horizon PD. For comparison purpose, we also included the results from two additional PD models where a single horizon is adopted for both mechanical and thermal fields. Observably, when a horizon of  $\delta = \Delta x$  is used, reasonable results for temperature are obtained whereas the displacement is far from satisfactory. When a horizon of  $\delta = 3\Delta x$  is adopted, mechanical responses are well captured but the temperature is not in good agreement with the FEM results. The results justify the necessity of adopting multi horizons for different physical fields. Furthermore, we examine the temperature contours obtained from the multi-horizon thermomechanical PD model with comparison to the original PD model (i.e., where a single horizon is used) as shown in Fig. 11. The results from original PD model exhibit significant oscillations due to the reasons described in Section 3. In contrast, the temperature contours from the multi-horizon PD model are clearly smooth and noise-free. Hence, the results prove the capability of the multi-horizon PD approach in accurately modeling both the mechanical and thermal fields by utilization of distinct horizons to capture non-local and local responses effectively.

### 5.2. Thermomechanical response of 3D beam under thermal loading

A thermomechanical model for a 3D beam has been created to further test the performance of the proposed multi-horizon PD as shown in Fig. 12. One end of the beam is subjected to a constant temperature boundary condition where the temperature is kept at 1 °C and the other end of the beam is fixed. The beam has dimensions of 1m  $\times$  1m  $\times$  4m and is discretized into 62,500 uniform material points, with each point having a size of 4 cm. The temperature boundary is applied by one additional layer of material points (625

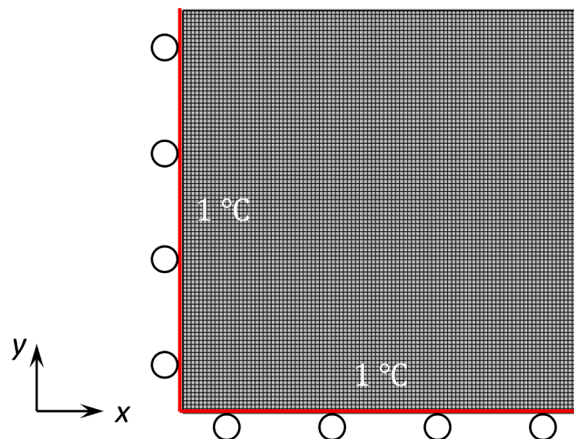


Fig. 8. Mesh and boundary conditions of a 2D slab.

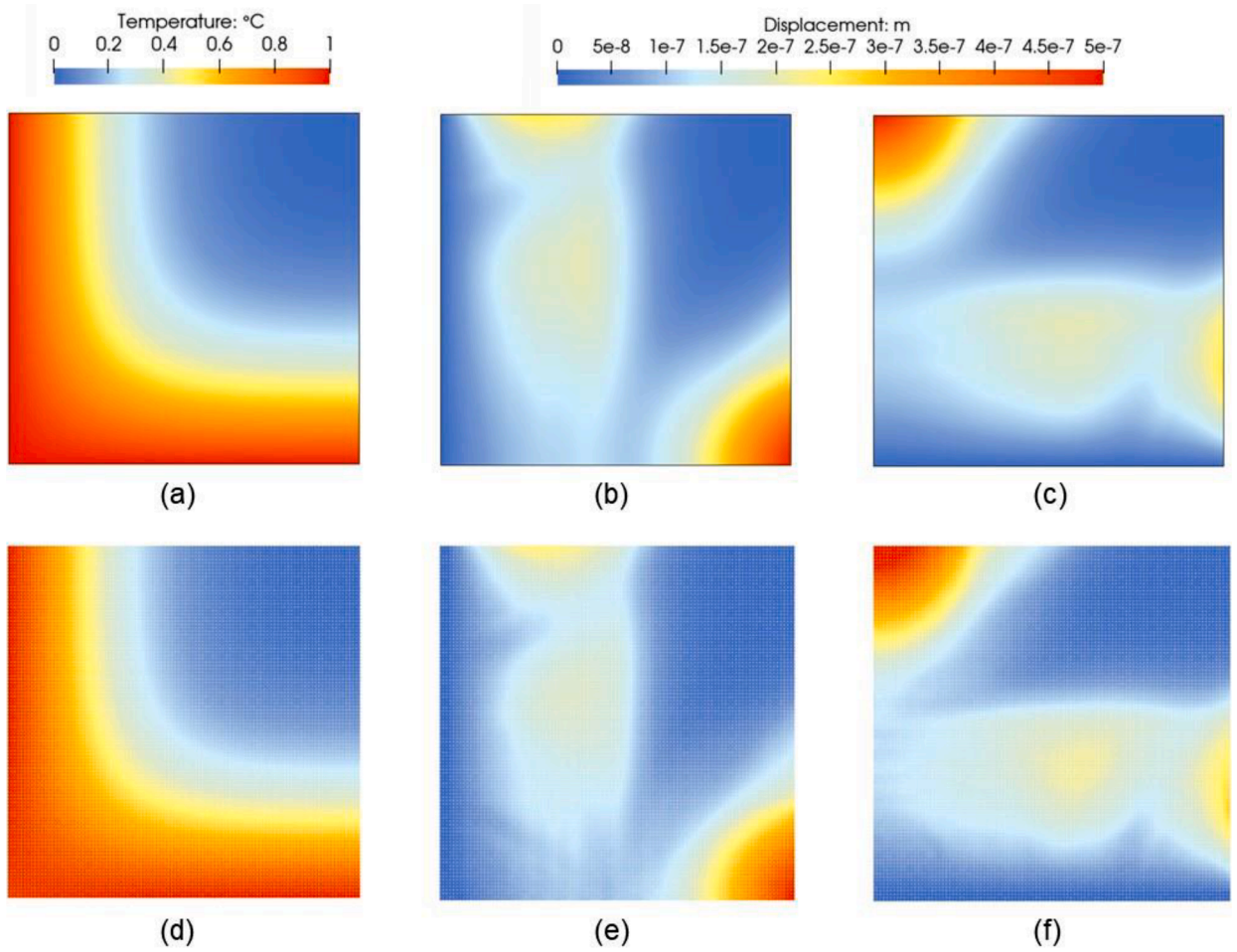


Fig. 9. Results obtained from FEM for: (a) temperature; (b) displacement in x direction; (c) displacement in y direction; and results obtained by multi-horizon PD for: (d) temperature; (e) displacement in x direction; (f) displacement in y direction.

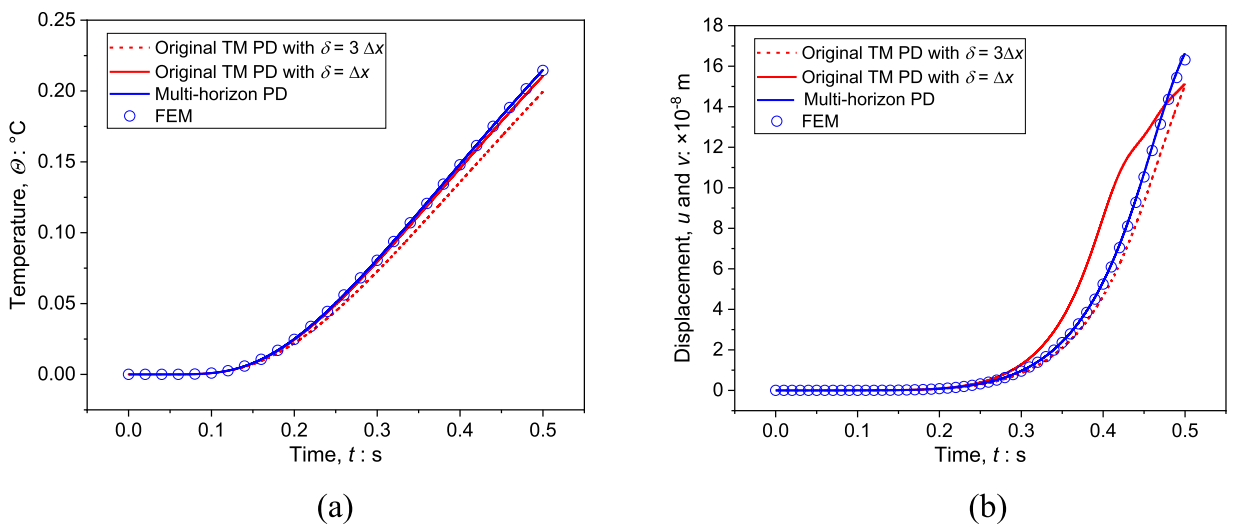


Fig. 10. Evolutions of: (a) temperature and (b) displacement magnitude at point (0.5,0.5) ( $u$  and  $v$  represent displacement along  $x$  and  $y$  directions, respectively).

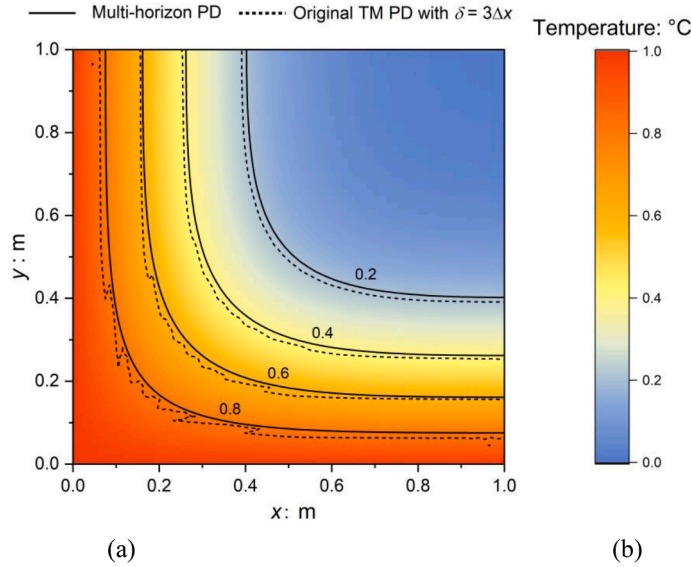


Fig. 11. Temperature contours of multi-horizon PD and original PD at  $t = 0.5$  s.

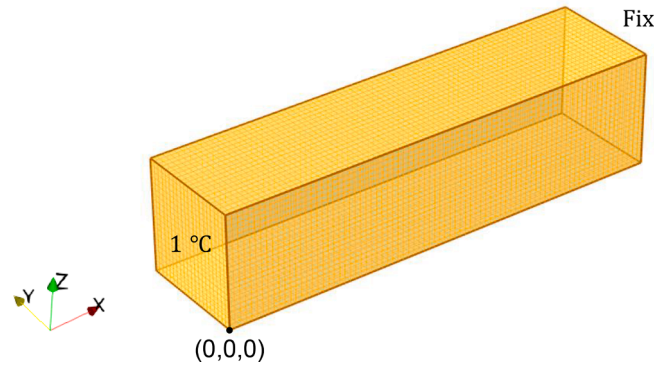


Fig. 12. Mesh and boundary conditions of a 3D beam.

material points) outside the left surface of the beam. All the material parameters used in the 3D case are the same as those used in the 2D case in the last section except for thermal conductivity  $k_{th}$ , which is set to  $1 \text{ W}/(\text{m}\cdot^\circ\text{C})$ . Again, the horizon is taken to be  $\delta = 3\Delta x$ , while the thermal horizon is adopted as  $\delta' = \Delta x$ .

The obtained results are presented in Fig. 13. Significant temperature noise can be observed both along the length and inside the beam when employing the original thermomechanical PD. Further examination of the temperature distribution at various cross-sections is given in Fig. 14(a)–(d). The observed temperature noise, primarily resulting from the truncation error and excessive number of neighbors, appears to manifest as a random pattern. With the introduction of the multi-horizon scheme, the oscillation is significantly mitigated and much smoother temperature profiles both along and inside the beam are obtained as shown in Figs. 13(d)–(f) and 14(e)–(f).

Quantitative comparisons with FEM results at the point  $(1, 0.25, 0.25)$  are depicted in Fig. 15. The FEM results are obtained from COMSOL Multiphysics. The multi-horizon PD demonstrates superior performance compared to the original thermomechanical PD method, regardless of whether a horizon size of  $\delta = 3\Delta x$  or  $\delta = \Delta x$  is used. Moreover, the multi-horizon method seems to offer even smoother results for in the displacements in  $x$  direction than FEM as can be seen in Fig. 15(b).

### 5.3. Fully coupled responses of plate subjected to combined force and temperature

Although based on the fully coupled multi-horizon PD method, the above two cases only involve thermally induced thermal and mechanical responses. The case in this section will focus on a plate subjected to coupled thermal and mechanical loads. As shown in Fig. 16, the left boundary of the plate is subjected to a  $1 \text{ Pa}$  normal pressure and a constant temperature equal to  $1 \text{ }^\circ\text{C}$ , while the right boundary is fixed along the  $x$  direction. The geometry of the plate and discretization are the same as the 2D case in Section 5.1. The

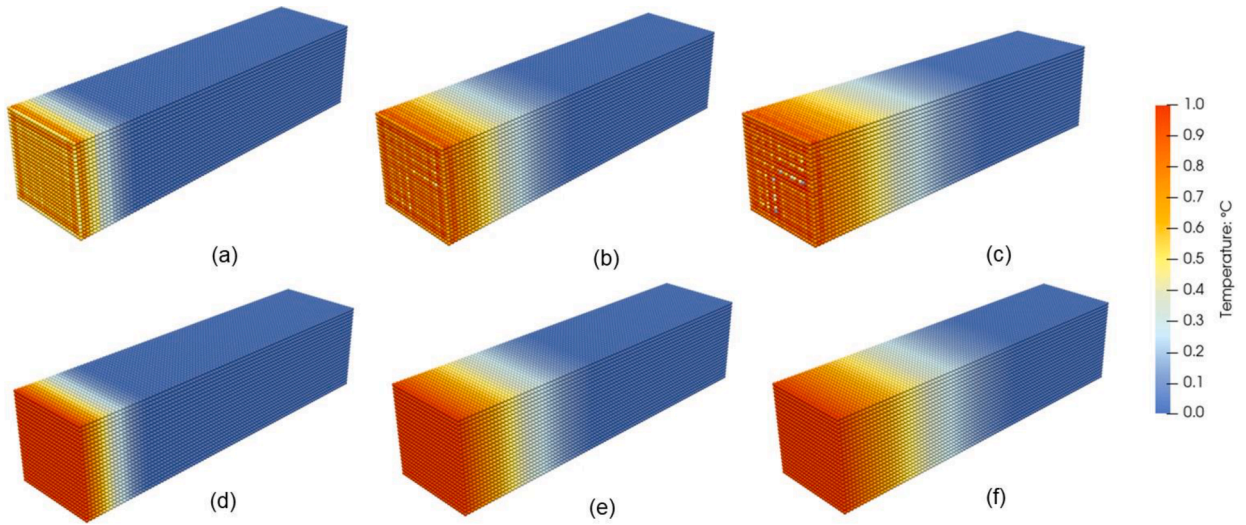


Fig. 13. Temperature colormap obtained from original TM PD at (a)  $t = 0.1$  s; (b)  $t = 0.5$  s; (c)  $t = 1$  s; and from multi-horizon PD at (d)  $t = 0.1$  s; (e)  $t = 0.5$  s; (f)  $t = 1$  s.

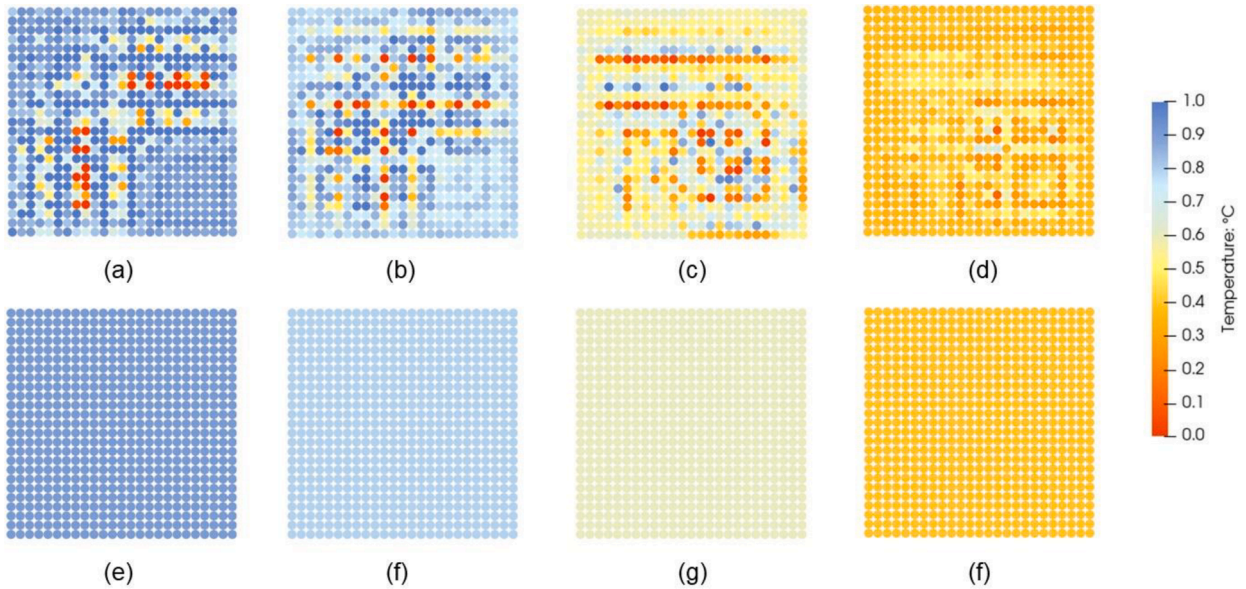


Fig. 14. Snapshots of temperature distribution at different cross-sections obtained from original TM PD: (a)  $x = 0.2$ ; (b)  $x = 0.5$ ; (c)  $x = 1.0$ ; (d)  $x = 1.7$ ; and from multi-horizon PD (e)  $x = 0.2$ ; (f)  $x = 0.5$ ; (g)  $x = 1.0$ ; (h)  $x = 1.7$ .

material parameters used are summarized as follows: density  $\rho = 1 \text{ kg/m}^3$ , Young’s modulus  $E = 1 \text{ Pa}$ , Poisson’s ratio  $\mu = 0.25$ , liner thermal expansion coefficient  $\beta = 1 \times 10^{-6} \text{ }^\circ\text{C}^{-1}$ , specific heat capacity  $c = 1 \text{ J/(kg}\cdot^\circ\text{C)}$ , thermal conductivity  $k_h = 0.5 \text{ W/(m}\cdot^\circ\text{C)}$ . Again, the horizon is taken to be  $\delta = 3\Delta x$ , while the thermal horizon is adopted as  $\delta' = \Delta x$ .

The same problem was analysed by Hosseini-Tehrani and Eslami (2000) using boundary element method (BEM), and therefore their results are used to verify the proposed multi-horizon scheme. Results of the simulation are presented in Fig. 17 for the evolution of temperature and magnitude of displacement for a point at (0.2, 0.5). The results obtained from the multi-horizon PD are in good agreement with the BEM results with respect to both temperature and displacement, confirming the capacity of the proposed method in simulating fully coupled thermo-mechanical response of material.

#### 5.4. Thermally induced fracturing in granite

To further demonstrate the capability of the proposed multi-horizon PD in modeling the fracturing process induced by various

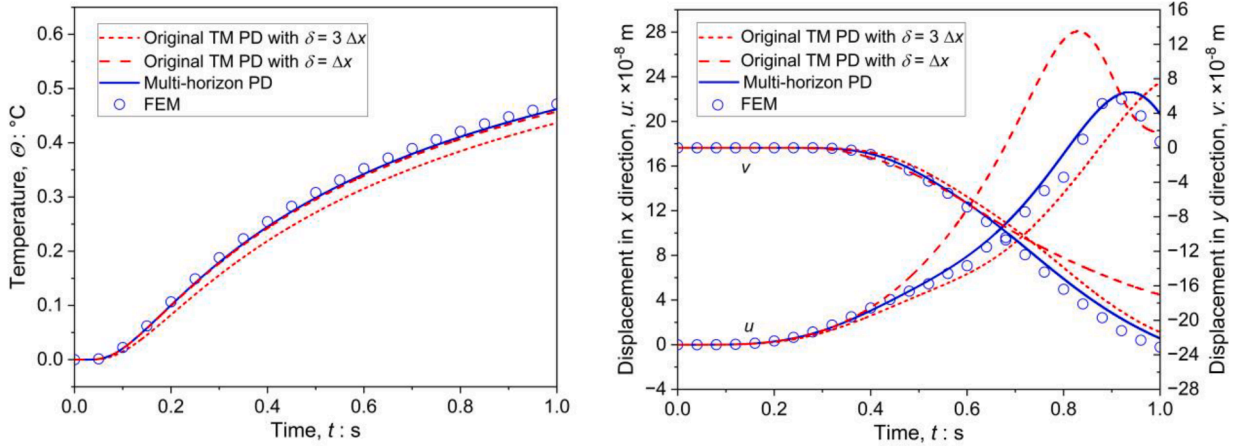


Fig. 15. Evolutions of: (a) temperature and (b) displacements at point (1, 0.25, 0.25) ( $u$  and  $v$  represent displacement along  $x$  and  $y$  directions, respectively).

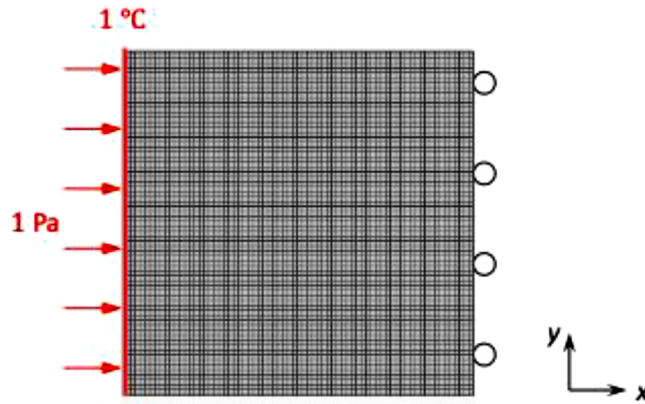


Fig. 16. Model of a 2D plate subject to combined thermal and mechanical loadings.

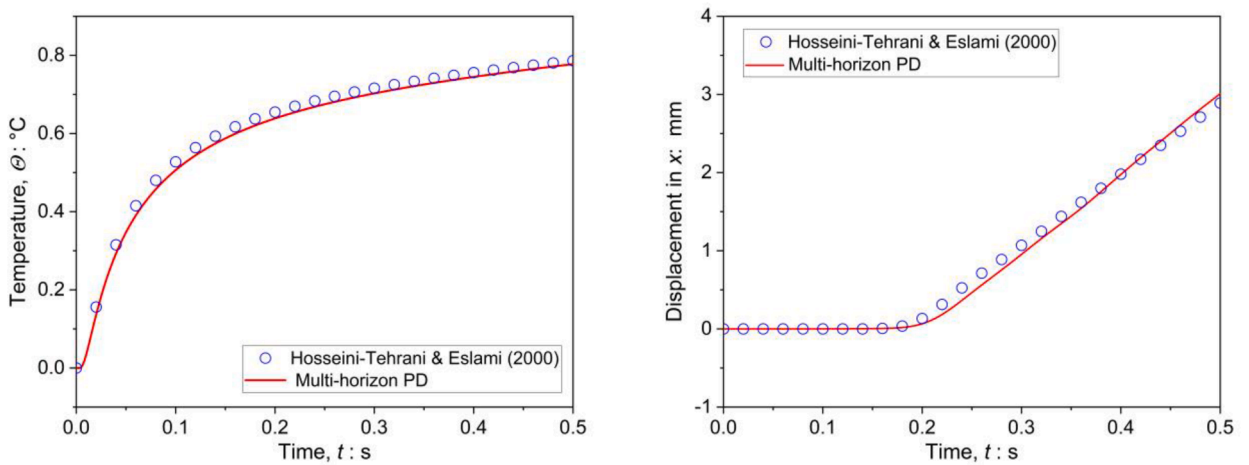


Fig. 17. Evolutions of: (a) temperature and (b) displacement magnitude at point (0.2, 0.5).

physical fields beyond mechanical loading, the thermally induced fracturing in an unconfined granite is modeled. The model setup follows an experiment conducted on Lac Du Bonnet (LDB) granite (Jansen et al., 1993), which has a density of  $2650 \text{ kg/m}^3$ , an elastic modulus of  $67 \text{ GPa}$ , a Poisson’s ratio of  $0.33$ , a thermal expansion coefficient of  $3.5 \times 10^{-6} \text{ }^\circ\text{C}^{-1}$ , a specific heat of  $1015 \text{ J/kg/}^\circ\text{C}$ , and a thermal conductivity of  $3.5 \text{ W/m/}^\circ\text{C}$ . The rock specimen is a  $15\text{-cm}$  cube with a  $1\text{-cm}$ -diameter vertical borehole drilled at the center of the specimen, which can be well simplified into a 2D plane strain numerical model as shown in Fig. 18(c). The numerical model is discretized into  $22,384$  material points, with each material point size equal to  $1 \text{ mm}$ . Note that the mesh is not totally symmetric owing to the fact that the granite in experiment is not isotropic and homogenous. The granite is modeled by the multi-horizon PD with horizon set as three times the material point size and thermal horizon set as  $1.2$  times the material point size, along with the critical stretch damage model and tension failure model as described in Section 2.3. The critical energy release rate and tensile strength of LDB granite are adopted as  $70 \text{ J/m}^2$  (Wang et al., 2018b) and  $9 \text{ MPa}$  (Martin, 1994), respectively. Note that the critical energy release rate and, consequently, the critical stretch can both be temperature dependent. For example, the fracture toughness of granite was found to decrease with rising temperature (Feng et al., 2019; Ge et al., 2021). Nonetheless, such effect is apparent only after a long duration heating process. In the present study, all the material properties are assumed to be temperature-independent constants. When necessary, the temperature-dependency of material fracture strength can be further considered by incorporating a relationship between temperature and critical energy release rate into the damage model presented in Section 2.3. The initial temperature and temperature of the four outer boundaries of the model are set as  $20 \text{ }^\circ\text{C}$ , while thermal loading with a rate of  $0.05 \text{ }^\circ\text{C/s}$  is applied on the inner circular boundary. Simulation is performed to  $2,000 \text{ s}$  with time step of  $2 \times 10^{-7} \text{ s}$ .

Fig. 19 shows the distribution of several crucial variables, including temperature, displacement in  $x$  direction, damage and major principal stress at different times. As the temperature applied to the borehole increases, heat is conducted from the inner boundary towards the outer boundary. This results in the formation of compressive stress near the borehole, while tensile stress is induced in certain areas of the free surface. These stresses result from temperature gradient between inner and outer part of the model and relatively high transverse thermal expansion of inner part with respect to outer part. When the borehole is heated to  $102.88 \text{ }^\circ\text{C}$  at about  $1657.6 \text{ s}$ , the tensile stress exceeds the tensile strength of the granite and therefore fracture is initiated from the outer surface first. Extensive tests conducted by Jackson et al. (1989) reported that the critical fracture temperature for LDB granite falls in the range of  $80\text{ }^\circ\text{C}$ - $125\text{ }^\circ\text{C}$ , which concurs with the numerical results. Once the initial crack forms, the tensile stress becomes localized at the crack front, which drives the crack to propagate continuously, while the tensile stress at other positions tends to dissipate. Additionally, a significant jump in displacement is observed along the two sides of the crack. This displacement jump is a result of the release of stored elastic energy during crack propagation. With further increase in temperature, a second crack is initiated at the lower surface and the two cracks finally propagate nearly parallelly to the edge of borehole. The fracturing pattern is consistent with that reported by literatures (Jackson et al., 1989; Jansen et al., 1993), and the morphology of crack as shown in Fig. 19 match well with the test results given in Fig. 18(b). The presence of the crack hinders the conduction of heat but does not completely interrupt it. As depicted in the top-right figure of Fig. 19, heat is still able to transfer outwards after the penetration cracks have formed. However, the temperature distributions on different sides of the crack are no longer symmetric due to the hindrance caused by the crack. The asymmetry in temperature distribution is a direct consequence of the presence and effects of the crack on the heat transfer process. This example well demonstrates the capability of the multi-horizon PD in modeling evolving discontinuities subject to thermal loading.

6. Conclusions and discussion

This paper presents a new fully coupled thermomechanical state-based PD model that combines non-local operators to solve the heat conduction equation with a thermoelastic PD solid model. The dispersion analysis based on spectral approach and error analysis based on Taylor expansion reveal that using large horizons induces more error and noise, resulting in a decrease in the conduction rate.

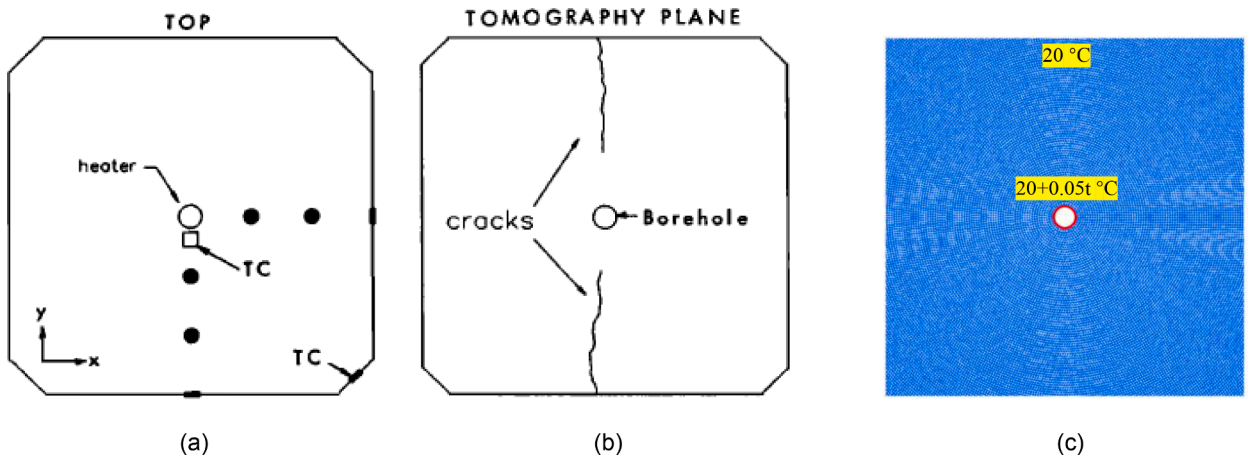


Fig. 18. (a) Experiment setup (Jansen et al., 1993); (b) Sketches of major fractures in the experiment (Jansen et al., 1993); and (c) Numerical model.

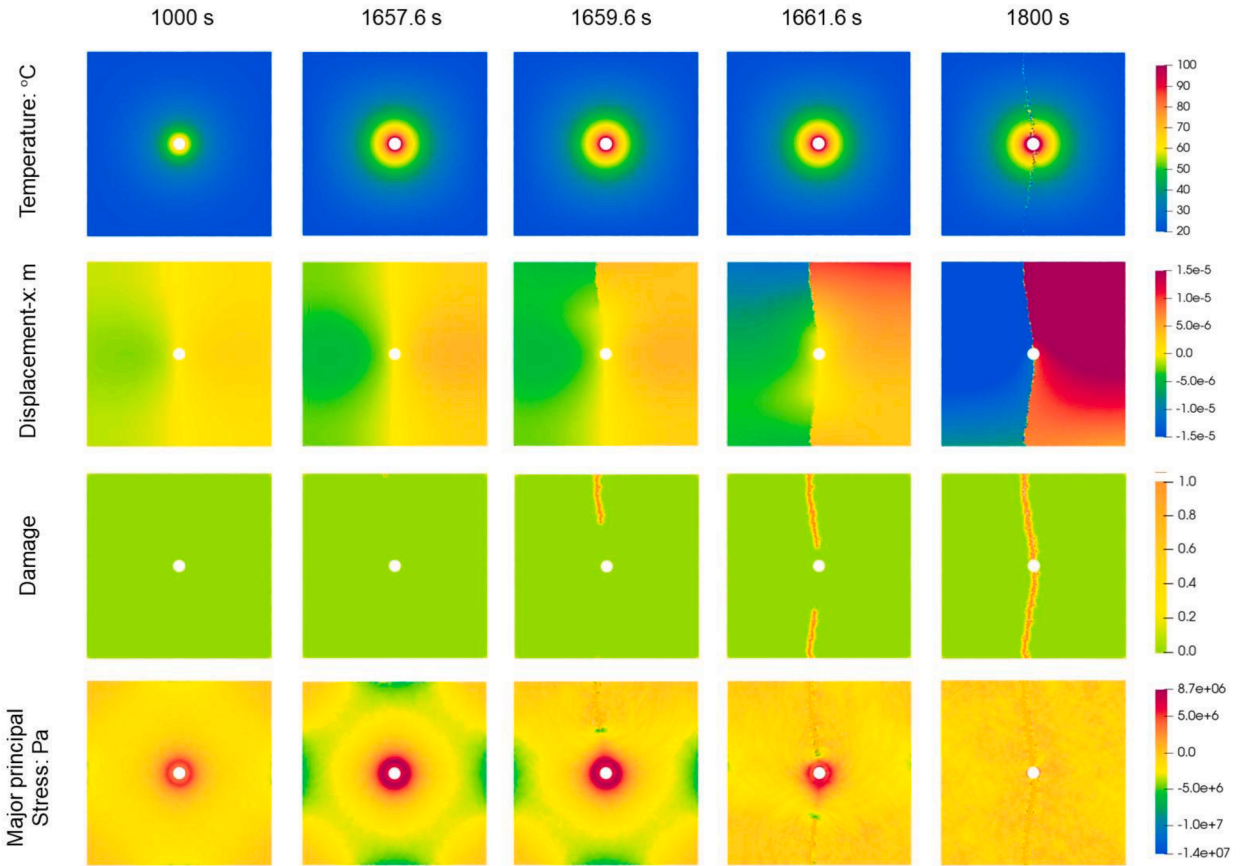


Fig. 19. Evolutions of temperature, displacement in x direction, damage and major principal stress at different times.

To address this issue, this paper proposes an innovative multi-horizon scheme that uses different horizons for different physical fields. For thermomechanical cases, a smaller horizon for thermal field and a larger horizon for the mechanical field are adopted to ensure the accuracy of heat conduction simulation while maintaining the capability of capturing non-local effects in mechanical responses. The numerical results show that the multi-horizon scheme offers noise-free and more accurate solutions. The scheme allows for the adoption of distinct horizon sizes that are most suitable for capturing the specific characteristics and phenomena associated with a particular physical field and serves a useful tool when coupling different physical fields in PD. Although the presented approach focuses on the TM PD, the generality of this paper is not lost owing to the complete analogy between different physical fields within solid (Mitchell and Soga, 2005). The presented approach can indeed be used to derive more sophisticated multi-physics PD-based computational framework in the future, including but not limited to coupled hydromechanical, electromechanical, and mechanical-chemical processes.

Due to limited length of this paper, it has not been possible to exhaustively explore all aspects of the multi-horizon PD. One potential issue that requires further investigation is the mesh dependency of the model. The presented numerical examples utilize a uniform mesh for optimal performance. However, when using an irregular discretization pattern, instability issues may arise, particularly when dealing with physical fields other than the mechanical field. This might be partially attributed to the poor evaluation of derivatives from integration over irregularly distributed material points. Further efforts are needed to study the influence of mesh on numerical stability. Additionally, in scenarios involving coupled heat contact and cracking problems across different materials or phases, the development of a multi-resolution scheme (Yao et al., 2023; Wang et al., 2022b) may become necessary. However, this topic is beyond the scope of the current study and will be addressed separately in future research. Another concern is the computational cost for the pure PD-based framework, particularly for 3D simulations with a large material stiffness and a small thermal conductivity. In such scenarios, a small time step may be necessary which would trigger overwhelming computational cost. Adopting an implicit scheme and/or GPU-based parallel computing may be beneficial. In addition, coupling PD with local methods such as FEM (Ni et al., 2021, 2022) may also be advantageous for saving computational cost by splitting computations of different physical fields between PD and other methods.

## CRediT authorship contribution statement

**Changyi Yang:** Conceptualization, Methodology, Software, Data curation, Writing – original draft. **Fan Zhu:** Software, Validation, Visualization, Writing – review & editing. **Jidong Zhao:** Conceptualization, Supervision, Investigation, Validation, Writing – review & editing, Funding acquisition.

## Declaration of competing interest

The authors declare that they have no known competing financial interests or personal relationships that could have appeared to influence the work reported in this paper.

## Data availability

Data will be made available on request.

## Acknowledgments

The study was financially supported by the National Science Foundation of China under project 11972030, Research Grants Council of Hong Kong (through GRF project 16208720, CRF project C7082-22G, TRS project T22-606/23-R, and HKUST SSTSP FP907), and Hetao Shenzhen-Hong Kong Science and Technology Innovation Cooperation Zone (HZQBKCZYB2020083). Fan Zhu acknowledges support from JSPS KAKENHI Grant Number 23K13403. Changyi Yang acknowledges financial support from the Hong Kong Ph.D. Fellowship Scheme funded by Research Grants Council of Hong Kong and would like to express gratitude to Prof. Erdogan Madenci from the University of Arizona, and Prof. Heng Zhang from Hohai University for the beneficial discussions.

## Supplementary materials

Supplementary material associated with this article can be found, in the online version, at [doi:10.1016/j.jmps.2024.105758](https://doi.org/10.1016/j.jmps.2024.105758).

## References

- Agwai, A. G. (2011). A peridynamic approach for coupled fields. <https://repository.arizona.edu/handle/10150/204892>.
- Bazant, Z.P., Luo, W., Chau, V.T., Bessa, M.A., 2016. Wave dispersion and basic concepts of peridynamics compared to classical nonlocal damage models. *J. Appl. Mech.* 83 (11), 111004 <https://doi.org/10.1115/1.4034319>.
- Bazazzadeh, S., Mossaiby, F., Shojaei, A., 2020. An adaptive thermo-mechanical peridynamic model for fracture analysis in ceramics. *Eng. Fract. Mech.* 223, 106708 <https://doi.org/10.1016/j.engfracmech.2019.106708>.
- Bergel, G.L., Li, S., 2016. The total and updated lagrangian formulations of state-based peridynamics. *Comput. Mech.* 58 (2), 351–370. <https://doi.org/10.1007/s00466-016-1297-8>.
- Bessa, M.A., Foster, J.T., Belytschko, T., Liu, W.K., 2014. A meshfree unification: reproducing kernel peridynamics. *Comput. Mech.* 53 (6), 1251–1264. <https://doi.org/10.1007/s00466-013-0969-x>.
- Buckman, S., Morris, R.H., Bourman, R.P., 2021. Fire-induced rock spalling as a mechanism of weathering responsible for flared slope and inselberg development. *Nat. Commun.* 12 (1) <https://doi.org/10.1038/s41467-021-22451-2>. Article 1.
- Butt, S.N., Timothy, J.J., Meschke, G., 2017. Wave dispersion and propagation in state-based peridynamics. *Comput. Mech.* 60 (5), 725–738. <https://doi.org/10.1007/s00466-017-1439-7>.
- Chang, H., Chen, A., Kareem, A., Hu, L., Ma, R., 2022. Peridynamic differential operator-based Eulerian particle method for 2D internal flows. *Comput. Methods Appl. Mech. Eng.* 392, 114568 <https://doi.org/10.1016/j.cma.2021.114568>.
- Chen, W., Gu, X., Zhang, Q., Xia, X., 2021. A refined thermo-mechanical fully coupled peridynamics with application to concrete cracking. *Eng. Fract. Mech.* 242, 107463 <https://doi.org/10.1016/j.engfracmech.2020.107463>.
- Chen, Z., Bobaru, F., 2015. Peridynamic modeling of pitting corrosion damage. *J. Mech. Phys. Solids* 78, 352–381. <https://doi.org/10.1016/j.jmps.2015.02.015>.
- Feng, G., Kang, Y., Wang, X., 2019. Fracture failure of granite after varied durations of thermal treatment: an experimental study. *R. Soc. Open Sci.* 6 (7), 190144 <https://doi.org/10.1098/rsos.190144>.
- Gao, Y., Oterkus, S., 2019. Fully coupled thermomechanical analysis of laminated composites by using ordinary state based peridynamic theory. *Compos. Struct.* 207, 397–424. <https://doi.org/10.1016/j.compstruct.2018.09.034>.
- Gao, Y., Oterkus, S., 2020. Fluid-elastic structure interaction simulation by using ordinary state-based peridynamics and peridynamic differential operator. *Eng. Anal. Bound. Elem.* 121, 126–142. <https://doi.org/10.1016/j.enganabound.2020.09.012>.
- Ge, Z., Sun, Q., Yang, T., Luo, T., Jia, H., Yang, D., 2021. Effect of high temperature on mode-I fracture toughness of granite subjected to liquid nitrogen cooling. *Eng. Fract. Mech.* 252, 107834 <https://doi.org/10.1016/j.engfracmech.2021.107834>.
- Gu, X., Zhang, Q., Huang, D., Yv, Y., 2016. Wave dispersion analysis and simulation method for concrete SHPB test in peridynamics. *Eng. Fract. Mech.* 160, 124–137. <https://doi.org/10.1016/j.engfracmech.2016.04.005>.
- Ha, Y.D., Bobaru, F., 2010. Studies of dynamic crack propagation and crack branching with peridynamics. *Int. J. Fract.* 162 (1), 229–244. <https://doi.org/10.1007/s10704-010-9442-4>.
- Hahn & Özisik. (2012). Heat conduction.
- Hosseini-Tehrani, P., Eslami, M.R., 2000. BEM analysis of thermal and mechanical shock in a two-dimensional finite domain considering coupled thermoelasticity. *Eng. Anal. Bound. Elem.* 24 (3), 249–257. [https://doi.org/10.1016/S0955-7997\(99\)00063-6](https://doi.org/10.1016/S0955-7997(99)00063-6).
- Jackson, R., Lau, J.S.O., Annor, A., 1989. Mechanical, thermo-mechanical and joint properties of rock samples from the site of AECL's underground research laboratory, Lac du Bonnet, Manitoba. *Materials: from theory to practice*. In: *Proceedings of the 42nd Canadian Geotechnical Conference, Winnipeg*. Canadian Geotechnical Society. Toronto, pp. 41–49.

- Jansen, D.P., Carlson, S.R., Young, R.P., Hutchins, D.A., 1993. Ultrasonic imaging and acoustic emission monitoring of thermally induced microcracks in Lac du Bonnet granite. *J. Geophys. Res. Solid Earth* 98 (B12), 22231–22243. <https://doi.org/10.1029/93JB01816>.
- Kilic, B., Madenci, E., 2010. Peridynamic theory for thermomechanical analysis. *IEEE Trans. Adv. Packag.* 33 (1), 97–105. <https://doi.org/10.1109/TADVP.2009.2029079>.
- Kulkarni, S., Tabarraei, A., 2018. An analytical study of wave propagation in a peridynamic bar with nonuniform discretization. *Eng. Fract. Mech.* 190, 347–366. <https://doi.org/10.1016/j.engfracmech.2017.12.019>.
- Le, Q.v., Chan, W.k., Schwartz, J., 2014. A two-dimensional ordinary, state-based peridynamic model for linearly elastic solids. *Int. J. Numer. Methods Eng.* 98 (8), 547–561. <https://doi.org/10.1002/nme.4642>.
- Liu, X., Yu, P., Zheng, B., Oterkus, E., He, X., Lu, C., 2024. Prediction of graphene's mechanical and fracture properties via peridynamics. *Int. J. Mech. Sci.* 266, 108914. <https://doi.org/10.1016/j.ijmecsci.2023.108914>.
- Madenci, E., Barut, A., Dorduncu, M., 2019. *Peridynamic Differential Operator for Numerical Analysis*. Springer International Publishing. <https://doi.org/10.1007/978-3-030-02647-9>.
- Madenci, E., Oterkus, E., 2014. *Peridynamic Theory and Its Applications*. Springer, New York. <https://doi.org/10.1007/978-1-4614-8465-3>.
- Martin, C.D., 1994. *The Strength of Massive Lac du Bonnet Granite Around Underground Openings*. National Library of Canada = Bibliothèque nationale du Canada.
- Menon, S., Song, X., 2021. A stabilized computational nonlocal poromechanics model for dynamic analysis of saturated porous media. *Int. J. Numer. Methods Eng.* 122 (20), 5512–5539. <https://doi.org/10.1002/nme.6762>.
- Menon, S., Song, X., 2022. Computational multiphase periporomechanics for unguided cracking in unsaturated porous media. *Int. J. Numer. Methods Eng.* 123 (12), 2837–2871. <https://doi.org/10.1002/nme.6961>.
- Menon, S., Song, X., 2023. Computational coupled large-deformation periporomechanics for dynamic failure and fracturing in variably saturated porous media. *Int. J. Numer. Methods Eng.* 124 (1), 80–118. <https://doi.org/10.1002/nme.7109>.
- Mikata, Y., 2012. Analytical solutions of peristatic and peridynamic problems for a 1D infinite rod. *Int. J. Solids Struct.* 49 (21), 2887–2897. <https://doi.org/10.1016/j.jisolsolstr.2012.02.012>.
- Mitchell, J. K., & Soga, K. (n.d.). *Fundamentals of Soil Behavior*. 2005.
- Monaghan, J.J., 1994. Simulating free surface flows with SPH. *J. Comput. Phys.* 110 (2), 399–406. <https://doi.org/10.1006/jcph.1994.1034>.
- Ni, T., Fan, X., Zhang, J., Zaccariotto, M., Galvanetto, U., Schrefler, B.A., 2023. A peridynamic-enhanced finite element method for thermo-hydro-mechanical coupled problems in saturated porous media involving cracks. *Comput. Methods Appl. Mech. Eng.* 417, 116376. <https://doi.org/10.1016/j.cma.2023.116376>.
- Ni, T., Sanavia, L., Zaccariotto, M., Galvanetto, U., Schrefler, B.A., 2022. Fracturing dry and saturated porous media, Peridynamics and dispersion. *Comput. Geotech.* 151, 104990. <https://doi.org/10.1016/j.compgeo.2022.104990>.
- Ni, T., Zaccariotto, M., Zhu, Q.Z., Galvanetto, U., 2021. Coupling of FEM and ordinary state-based peridynamics for brittle failure analysis in 3D. *Mech. Adv. Mater. Struct.* 28 (9), 875–890. <https://doi.org/10.1080/15376494.2019.1602237>.
- Oterkus, S., Madenci, E., Agwai, A., 2014a. Fully coupled peridynamic thermomechanics. *J. Mech. Phys. Solids* 64, 1–23. <https://doi.org/10.1016/j.jmps.2013.10.011>.
- Oterkus, S., Madenci, E., Agwai, A., 2014b. Peridynamic thermal diffusion. *J. Comput. Phys.* 265, 71–96. <https://doi.org/10.1016/j.jcp.2014.01.027>.
- Oterkus, S., Madenci, E., Oterkus, E., 2017. Fully coupled poroelastic peridynamic formulation for fluid-filled fractures. *Eng. Geol.* 225, 19–28. <https://doi.org/10.1016/j.enggeo.2017.02.001>.
- Rabczuk, T., Ren, H., Zhuang, X., 2019. A nonlocal operator method for partial differential equations with application to electromagnetic waveguide problem. *Comput. Mater. Contin.* 59 (1), 31–55. <https://doi.org/10.32604/cmc.2019.04567>.
- Ren, H., Zhuang, X., Cai, Y., Rabczuk, T., 2016. Dual-horizon peridynamics. *Int. J. Numer. Methods Eng.* 108 (12), 1451–1476. <https://doi.org/10.1002/nme.5257>.
- Ren, H., Zhuang, X., Rabczuk, T., 2020a. A higher-order nonlocal operator method for solving partial differential equations. *Comput. Methods Appl. Mech. Eng.* 367, 113132. <https://doi.org/10.1016/j.cma.2020.113132>.
- Ren, H., Zhuang, X., Rabczuk, T., 2020b. A nonlocal operator method for solving partial differential equations. *Comput. Methods Appl. Mech. Eng.* 358, 112621. <https://doi.org/10.1016/j.cma.2019.112621>.
- Ren, H., Zhuang, X., Timon, R., 2017. Dual-horizon peridynamics: a stable solution to varying horizons. *Comput. Methods Appl. Mech. Eng.* 318, 762–782. <https://doi.org/10.1016/j.cma.2016.12.031>.
- Ruan, H., Rezaei, S., Yang, Y., Gross, D., Xu, B.X., 2023. A thermo-mechanical phase-field fracture model: application to hot cracking simulations in additive manufacturing. *J. Mech. Phys. Solids* 172, 105169. <https://doi.org/10.1016/j.jmps.2022.105169>.
- Shi, K., Zhu, F., Zhao, J., 2022. Multi-scale analysis of shear behaviour of crushable granular sand under general stress conditions. *Géotechnique* 1–18. <https://doi.org/10.1680/jgeot.21.00412>.
- Silling, S.A., 2000. Reformulation of elasticity theory for discontinuities and long-range forces. *J. Mech. Phys. Solids* 48 (1), 175–209. [https://doi.org/10.1016/S0022-5096\(99\)00029-0](https://doi.org/10.1016/S0022-5096(99)00029-0).
- Silling, S.A., 2016. Solitary waves in a peridynamic elastic solid. *J. Mech. Phys. Solids* 96, 121–132. <https://doi.org/10.1016/j.jmps.2016.06.001>.
- Silling, S.A., Askari, E., 2005. A meshfree method based on the peridynamic model of solid mechanics. *Comput. Struct.* 83 (17), 1526–1535. <https://doi.org/10.1016/j.compstruc.2004.11.026>.
- Silling, S.A., Epton, M., Weckner, O., Xu, J., Askari, E., 2007. Peridynamic states and constitutive modeling. *J. Elast.* 88 (2), 151–184. <https://doi.org/10.1007/s10659-007-9125-1>.
- Song, X., Silling, S.A., 2020. On the peridynamic effective force state and multiphase constitutive correspondence principle. *J. Mech. Phys. Solids* 145, 104161. <https://doi.org/10.1016/j.jmps.2020.104161>.
- Song, Y., Li, S., Li, Y., 2022. Peridynamic modeling and simulation of thermo-mechanical fracture in inhomogeneous ice. *Eng. Comput.* <https://doi.org/10.1007/s00366-022-01616-7>.
- Song, Y., Li, S., Zhang, S., 2021. Peridynamic modeling and simulation of thermo-mechanical de-icing process with modified ice failure criterion. *Def. Technol.* 17 (1), 15–35. <https://doi.org/10.1016/j.dt.2020.04.001>.
- Sun, W., Fish, J., Guo, C., 2022a. Parallel PD-FEM simulation of dynamic fluid-driven fracture branching in saturated porous media. *Eng. Fract. Mech.* 274, 108782. <https://doi.org/10.1016/j.engfracmech.2022.108782>.
- Sun, W., Fish, J., Lin, P., 2022b. Numerical simulation of fluid-driven fracturing in orthotropic poroelastic media based on a peridynamics-finite element coupling approach. *Int. J. Rock Mech. Min. Sci.* 158, 105199. <https://doi.org/10.1016/j.ijrmm.2022.105199>.
- Sun, W., Susmel, L., Xie, P., 2023. Thermal fracturing in orthotropic rocks with superposition-based coupling of PD and FEM. *Rock Mech. Rock Eng.* 56 (3), 2395–2416. <https://doi.org/10.1007/s00603-022-03164-4>.
- Tu, Q., Li, S., 2017. An updated Lagrangian particle hydrodynamics (ULPH) for Newtonian fluids. *J. Comput. Phys.* 348, 493–513. <https://doi.org/10.1016/j.jcp.2017.07.031>.
- Wan, J., Chen, Z., Chu, X., Liu, H., 2020. Dependency of single-particle crushing patterns on discretization using peridynamics. *Powder Technol.* 366, 689–700. <https://doi.org/10.1016/j.powtec.2020.03.021>.
- Wang, H.F., 2017. *Theory of linear poroelasticity with applications to geomechanics and hydrogeology. Theory of Linear Poroelasticity with Applications to Geomechanics and Hydrogeology*. Princeton University Press. <https://doi.org/10.1515/9781400885688>.
- Wang, H., Oterkus, E., Oterkus, S., 2018a. Peridynamic modelling of fracture in marine lithium-ion batteries. *Ocean Eng.* 151, 257–267. <https://doi.org/10.1016/j.oceaneng.2018.01.049>.
- Wang, X., Wu, W., Zhu, H., Zhang, H., Lin, J.S., 2022a. Application of three-dimensional explicit discontinuous deformation analysis on wave propagation in rock masses using three viscous boundaries with the remedy for artificial joints. *Rock Mech. Rock Eng.* 55 (10), 5821–5843. <https://doi.org/10.1007/s00603-022-02931-7>.

- Wang, X., Wu, W., Zhu, H., Zhang, H., Lin, J.S., Bobet, A., 2022b. A global direct search method for high-fidelity contact detection between arbitrarily shaped three-dimensional convex polyhedral blocks. *Comput. Geotech.* 150, 104891. <https://doi.org/10.1016/j.compgeo.2022.104891>.
- Wang, Y., Zhou, X., Kou, M., 2018b. A coupled thermo-mechanical bond-based peridynamics for simulating thermal cracking in rocks. *Int. J. Fract.* 211 (1), 13–42. <https://doi.org/10.1007/s10704-018-0273-z>.
- Wang, Y., Zhou, X., Kou, M., 2019. An improved coupled thermo-mechanic bond-based peridynamic model for cracking behaviors in brittle solids subjected to thermal shocks. *Eur. J. Mech. A/Solids* 73, 282–305. <https://doi.org/10.1016/j.euromechsol.2018.09.007>.
- Wu, P., Chen, Z., 2023. Peridynamic electromechanical modeling of damaging and cracking in conductive composites: a stochastically homogenized approach. *Compos. Struct.* 305, 116528 <https://doi.org/10.1016/j.compstruct.2022.116528>.
- Xue, Y., Liu, S., Chai, J., Liu, J., Ranjith, P.G., Cai, C., Gao, F., Bai, X., 2023. Effect of water-cooling shock on fracture initiation and morphology of high-temperature granite: application of hydraulic fracturing to enhanced geothermal systems. *Appl. Energy* 337, 120858. <https://doi.org/10.1016/j.apenergy.2023.120858>.
- Yang, C., Li, L., Li, J., 2020. Service life of reinforced concrete seawalls suffering from chloride attack: theoretical modelling and analysis. *Constr. Build. Mater.* 263, 120172 <https://doi.org/10.1016/j.conbuildmat.2020.120172>.
- Yang, C., Zhu, F., Zhao, J., 2024. Coupled total- and semi-Lagrangian peridynamics for modelling fluid-driven fracturing in solids. *Comput. Methods Appl. Mech. Eng.* 419, 116580 <https://doi.org/10.1016/j.cma.2023.116580>.
- Yao, X., Chen, D., Wu, L., Huang, D., 2023. A multi-resolution DFPM-PD model for efficient solution of FSI problems with structural deformation and failure. *Eng. Anal. Bound. Elem.* 157, 424–440. <https://doi.org/10.1016/j.enganabound.2023.09.023>.
- Yu, J., Zhao, J., Liang, W., Zhao, S., 2024a. A semi-implicit material point method for coupled thermo-hydro-mechanical simulation of saturated porous media in large deformation. *Computer Methods in Applied Mechanics and Engineering* 418, 116462.
- Yu, J., Zhao, J., Liang, W., Zhao, S., 2024b. Multiscale modeling of coupled thermo-hydro-mechanical behavior in ice-bonded granular media subject to freeze-thaw cycles. *Computers and Geotechnics* 171, 106349.
- Yu, J., Zhao, J., Zhao, S., Liang, W., 2024c. Thermo-hydro-mechanical coupled material point method for modeling freezing and thawing of porous media. *Int. J. Numer. Anal. Methods Geomech.* <https://doi.org/10.1002/nag.3794>.
- Zhang, H., Qiao, P., 2018. An extended state-based peridynamic model for damage growth prediction of bimaterial structures under thermomechanical loading. *Eng. Fract. Mech.* 189, 81–97. <https://doi.org/10.1016/j.engfracmech.2017.09.023>.
- Zhang, H., Qiao, P., 2020. A two-dimensional ordinary state-based peridynamic model for elastic and fracture analysis. *Eng. Fract. Mech.* 232, 107040 <https://doi.org/10.1016/j.engfracmech.2020.107040>.
- Zhang, Y., Yu, S., Deng, H., 2023. Peridynamic model of deformation and failure for rock material under the coupling effect of multi-physical fields. *Theor. Appl. Fract. Mech.* 125, 103912 <https://doi.org/10.1016/j.tafmec.2023.103912>.
- Zhu, F., Zhao, J., 2019a. A peridynamic investigation on crushing of sand particles. *Géotechnique* 69 (6), 526–540. <https://doi.org/10.1680/jgeot.17.P.274>.
- Zhu, F., Zhao, J., 2019b. Modeling continuous grain crushing in granular media: a hybrid peridynamics and physics engine approach. *Comput. Methods Appl. Mech. Eng.* 348, 334–355. <https://doi.org/10.1016/j.cma.2019.01.017>.
- Zhu, F., Zhao, J., 2021. Peridynamic modelling of blasting induced rock fractures. *J. Mech. Phys. Solids* 153, 104469. <https://doi.org/10.1016/j.jmps.2021.104469>.